UNIVERSIDAD DE CHILE
FACULTAD DE CIENCIAS FÍSICAS Y MATEMÁTICAS
DEPARTAMENTO DE INGENIERÍA CIVIL

PARAMETRIC STUDY OF PIEZOELECTRIC-BASED RESONATORS IN METAMATERIALS DESIGN FOR BANDGAP GENERATION AND ENERGY HARVESTING

TESIS PARA OPTAR AL GRADO DE MAGÍSTER EN CIENCIAS DE LA INGENIERÍA, MENCIÓN INGENIERÍA ESTRUCTURAL, SÍSMICA Y GEOTÉCNICA

MEMORIA PARA OPTAR AL TÍTULO DE INGENIERO CIVIL

DIEGO ALEJANDRO ASTUDILLO LAGORIO

PROFESOR GUÍA:
RAFAEL RUIZ GARCÍA

MIEMBROS DE LA COMISIÓN:
VIVIANA MERUANE NARANJO
GAOFENG JIA

SANTIAGO DE CHILE
2022

RESUMEN DE LA MEMORIA PARA OPTAR
AL TÍTULO DE MAGÍSTER EN CIENCIAS
DE LA INGENIERÍA, MENCIÓN INGENIERÍA
ESTRUCTURAL, SÍSMICA Y GEOTÉCNICA
POR: DIEGO ALEJANDRO ASTUDILLO LAGORIO
FECHA: 2022
PROF. GUÍA: RAFAEL RUIZ GARCÍA

ESTUDIO PARAMÉTRICO DE RESONADORES BASADOS EN PIEZOELÉCTRICOS EN DISEÑO DE METAMATERIALES CON CAPACIDADES DE SUPRESIÓN DE VIBRACIONES Y RECOLECCIÓN DE ENERGÍA

Dentro del espectro de metamateriales, las estructuras periódicas son ampliamente estudiadas ya que pueden presentar bandgaps, los cuales corresponden a rangos de frecuencia en los que las ondas mecánicas se suprimen por completo. Recientemente, algunos autores han añadido piezoeléctricos a las estructuras periódicas con el objetivo de incorporar propiedades de recolección de energía. Este trabajo está motivado por la configuración 2D utilizada por Li et al. [1], en el que se combinan las propiedades de supresión de vibraciones y recolección de energía.

El objetivo de este trabajo es implementar un modelo de elementos finitos de una estructura periódica que sea capaz de presentar supresión de vibraciones y recolección de energía, y usarlo para ver la influencia de los parámetros del modelo en los bandgaps y la relación entre la recolección de energía y los bandgaps. Específicamente, se desarrolla un modelo de elementos finitos acoplados electromecánicamente de vigas de Bernoulli para modelar estructuras periódicas, que se componen de celdas unitarias cuadradas con voladizos con propiedades piezoeléctricas que se unen al marco estructural primario. A través de estos modelos se encuentra que el dominio de los vectores de onda que deben evaluarse en la condición periódica de Floquet-Bloch para identificar los bandgaps generados por los resonadores locales puede restringirse a solo 5 vectores de onda de la primera zona de Brillouin, lo que puede generar una gran disminución de los recursos computacionales al optimizar este tipo de configuración. Con base en este resultado, se realiza un análisis paramétrico para identificar la influencia de los parámetros del modelo en la ubicación y el tamaño de la banda prohibida. El análisis paramétrico se complementa con una variación simultánea de parámetros, lo que muestra los beneficios de la cuantificación de incertidumbres y algunas recomendaciones si se quiere desarrollar una optimización del bandgap producto de resonancias locales en este tipo de estructuras. Finalmente, se presentan funciones de respuesta de frecuencia de voltaje (FRF) para paneles finitos, que entregan resultados consistentes con lo estudiado a nivel de celda unitaria, y nos permite ver la relación entre la recolección de energía y la supresión de vibraciones.

RESUMEN DE LA MEMORIA PARA OPTAR
AL TÍTULO DE MAGÍSTER EN CIENCIAS
DE LA INGENIERÍA, MENCIÓN INGENIERÍA
ESTRUCTURAL, SÍSMICA Y GEOTÉCNICA
POR: DIEGO ALEJANDRO ASTUDILLO LAGORIO
FECHA: 2022
PROF. GUÍA: RAFAEL RUIZ GARCÍA

PARAMETRIC STUDY OF PIEZOELECTRIC-BASED RESONATORS IN METAMATERIALS DESIGN FOR BANDGAP GENERATION AND ENERGY HARVESTING

Within the spectrum of metamaterials, periodic structures are widely studied since they can present bandgaps, which correspond to frequency ranges in which mechanical waves are completely suppressed. Recently, some authors have added piezoelectrics to the periodic structures with the aim of incorporating energy harvesting properties. This work is motivated by the 2D configuration used by Li et al. [1], in which the properties of vibration suppression and energy harvesting are combined.

The objective of this work is to implement a finite element model of a periodic structure that is capable of presenting vibration suppression and energy harvesting, and use it to see the influence of the parameters on the bandgaps and the relationship between energy harvesting and bandgaps. Specifically, an electromechanically coupled finite element model of Bernoulli beams is developed to model periodic structures, which are composed of square unit cells with free-standing cantilevers featuring piezoelectric properties being attached to the primary structural frame. Through these models, it is found that the domain of the wave vectors that must be evaluated in the Floquet–Bloch periodic condition to identify bandgaps generated by local resonators can be restricted to only 5 wave vectors of the first Brillouin zone, which can generate a large decrease in computational resources when optimizing this type of configuration. Based on this result, a parametric analysis is performed to identify the influence of the model parameters on the location and size of the bandgap. The parametric analysis is complemented by a simultaneous variation of parameters, which shows the benefits of the quantification of uncertainties and some recommendations if you want to develop an optimization of the bandgap due to local resonances in this type of structures. Finally, voltage frequency response functions (FRF) for finite panels are presented, which deliver consistent results with what was studied at the unit cell level, and allows us to see the relationship between energy harvesting and vibration suppression.

Table of Content

List of Tables

List of Figures

Chapter 1

Introduction

Mechanical metamaterials [2–5] are artificial materials designed to achieve mechanical behaviors not found in nature, since their properties come from their microstructural design and differ from those of the material used in their composition (conventional materials such as metals or plastics are usually used). The objective performance includes static behaviors (such as negative thermal expansion [6], negative Poisson's ratio [7] and others) and dynamic behaviors (such as acoustic wave transmission with expected bandgaps or propagation paths [8–11], a unique combination of stiffness, strength and energy absorption performance [12], full-band mechanical vibration isolation [13], and others [14–16]).

For most vibration-isolation metamaterials, the magnitude of the energy flow will be suppressed after transmitting through them, while the direction remains unchanged [17–20]. To achieve this purpose, mechanical energy has to be dissipated [21–24], confined [25], or harvested and transferred to other forms [26, 27] by the metamaterials. Waves propagate in dynamic mechanical metamaterials only within specific frequency bands, referred to as pass bands, and they might be blocked within other frequency bands, which are called bandgaps. The mechanisms of mechanical metamaterials to intervene in the magnitude of mechanical waves strongly depend on their microstructure and could be divided into two main different phenomena at the micro-level [28]: Bragg scattering and Local Resonance.

Bragg scattering-type bandgaps require a lattice constant (i.e. cell periodicity) comparable to the wavelength of the bandgap, but by adding internal resonators (normally periodically) the elastic energy with specific frequency could be constrained [29], generating bandgaps that at lower frequencies than those of bragg scattering. Local resonators were originally investigated in the Maxwell–Rayleigh model [30]. Various continuous models, including extensional rods, Euler and Timoshenko beams [31] and so on have been discussed to illustrate the dynamic behaviors of materials containing local resonators [32].

From the first local resonant sonic crystals, an increasing number of acoustic metamaterials have been investigated based on the local resonant idea [33–36]. These materials could be applied to absorb impact energy [37], vibration suppression [38] and simultaneous vibration suppression and energy harvesting functions [1]. The external vibration energy could be trapped and transferred into the kinetic energy of the resonators and then further converted into electric energy through the mechano-electrical conversion, for example integrating piezoelectric elements.

There is much research on the formation and control of bandgaps due to electromechanical coupling in structures with piezoelectric layers [39–43]. It has been seen in the literature that when piezoelectrics are incorporated into periodic structures, they can have a double effect of energy harvesting and vibration attenuation [44–46]. Shen et al. demonstrated experimentally that the flat band of frequencies in metastructures can generate energy harvesting by adding piezoelectric patches [47]. This problem was theoretically investigated by Hu et al. for discrete [44] and continuous [48] structures, he also presented an extension of his work by coupling the internal resonators [49], which generated great improvements in energy harvesting and vibration suppression. This phenomenon was investigated experimentally by Li et al. [1] using a 3D printed panel, which corresponds to an extract of a periodic structure of a square unit cell with piezoelectric cantilevers at its vertices, similar to the configuration presented in figure 2.2. This configuration is very interesting since it can have various applications in the mechanical and civil industry (non-structural walls and machine enclosures/supports). The study of piezoelectric metamaterials for these applications is an incipient research field, since the studies have been restricted to 2D metastructures (frames) subjected to in-plane vibrations and no efforts have been made to achieve optimal designs.

A standard piezoelectric energy harvester (PEH) can convert dynamic deformations into electrical power when subjected to vibrations. The most common configuration consists of a unimorph cantilevered beam, which is composed of two layers, one that serves as structural support (substructure layer), and another that allows energy conversion (piezoelectric layer). Two piezoelectric layers can also be considered, which generates a bimorph configuration. A scheme of these configurations is shown in figure 1.1.

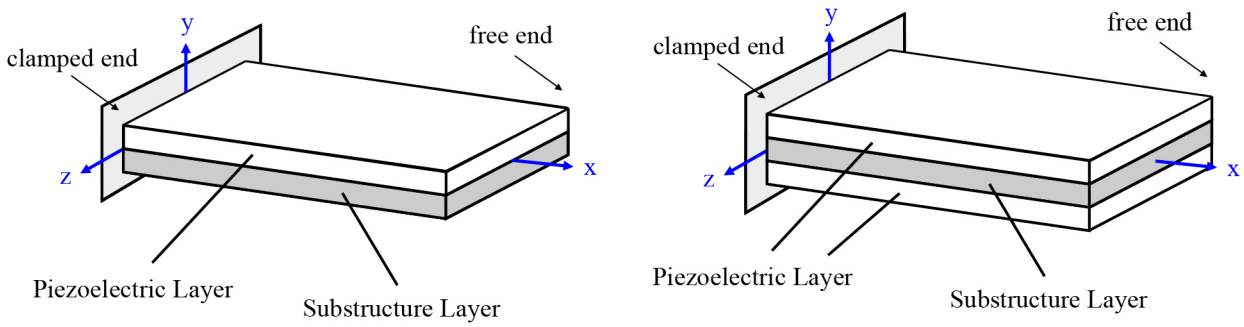

Figure 1.1: Scheme of **(a)** unimorph and **(b)** bimorph PEH.

Multiple models have been developed to describe and predict the PEHs electromechanical behavior, one of them is the model of Erturk and Inman, who presented the analytical distributed parameter solutions for unimorph [50] and bimorph [51] PEH configurations. Based on these models, De Marqui et al. [52] presented an electromechanical FE plate model for piezoelectric energy harvesting, and performed an optimization of piezoceramics incorporated in an unmanned air vehicle (UAV). Despite the development of high fidelity models, mismatches between numerical and experimental observations were detected by Peralta et al. [53] after studying the dynamic response of a group of PEHs with identical nominal elec-

tromechanical properties, raising the concern about the characterization of the uncertainties involved in the electromechanical properties. This is why it is interesting to find mechanisms to make efficient the repeated evaluation of models associated with metamaterials with piezoelectrics, which can generate a great saving of computational resources in the quantification of uncertainties and optimizations. In the case of periodic structures a source of savings may be to narrow the domain of the wave vectors that are evaluated in the Floquet–Bloch periodic condition [54].

The metamaterials used in this study are inspired by the configuration presented by Li et al. [1], so they correspond to periodic structures with square unit cells and incorporated bimorph PEH resonators. The questions that motivate this research are: How to increase the computational speed to characterize the bandgaps produced by local resonances? How do the physical and geometric parameters of the metamaterial influence the bandgap? What is the degree of dependence between energy harvesting and bandgap?

This research has 4 main objectives. The first is to develop and validate an electromechanically coupled finite element model using Bernoulli beam elements, to model periodic metamaterials formed by square unit cells with embedded piezoelectric-based bimorph resonators. The second consists of exploring different architectures to show that the domain of wave vectors that must be evaluated in the Floquet–Bloch periodic condition can be restricted to identify bandgaps generated by local resonators, which allows considerably reducing the computational cost of optimizations. The third consists of performing a parametric analysis based on the configuration shown in Li et al. [1] work, to see how the model parameters influence the bandgap. The fourth corresponds to seeing the degree of independence between the bandgap and the energy generation by calculating frequency response functions (FRFs) in panels made up of finite repetitions of the unit cells of the metamaterials.

The rest of the paper is organized as follows. Section 2 presents the metamaterial architecture used in the rest of the paper. Section 3 presents the numerical electromechanically coupled finite element model and its validation. Section 4 presents an analysis of the wave vectors that must be considered to know the size and location of the bandgaps due to local resonances, saving computational resources. Section 5 present a parametric study. Section 6 presents the combined effect of the variation of several parameters simultaneously, and some borderline cases that try to optimize the bandgap according to the results of the parametric analysis. Section 7 presents numerical examples of frequency response functions (FRF) on finite panels. Section 8 concludes the study.

Chapter 2

Metamaterial Architecture

Periodic structures are those obtained from the tessellation of a unit cell and can be described by a lattice called direct lattice, which is a regular arrangement of discrete points that are defined through vectors called direct lattice vectors, which must satisfy that for any point $\mathbf{x}$ of the lattice the distribution of points must be the same as when observed from another point $\tilde{\mathbf{x}}$ obtained from a displacement corresponding to a linear combination of the lattice vectors. In the two-dimensional case only 2 lattice vectors are required, then the mentioned property corresponds to $\tilde{\mathbf{x}} = \mathbf{x} + n_1\mathbf{e_1} + n_2\mathbf{e_2}$, where $\mathbf{e_1}$ and $\mathbf{e_2}$ are the direct lattice vectors, and n_1 and n_2 are integer weights. An example of direct lattice is shown in figure 2.1, in which the lattice vectors and the unit cell are shown. In the case of two-dimensional lattice, there are 5 arrangements that meet the requirements presented which are called Bravais lattices (oblique, rectangular, rhomboid, square, and hexagonal).

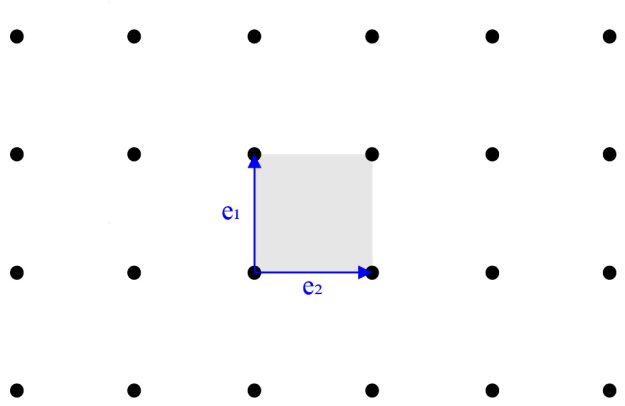

Figure 2.1: Extract from a square lattice of vectors $\mathbf{e_1}$ and $\mathbf{e_2}$, the unit cell is shown shaded.

The periodic cellular structures that are studied in later sections consist of two-dimensional panels made up of beams and cantilevers based on square unit cells as shown in figure 2.2. The cantilevers act as internal resonators and 2 layers of piezoelectric material are added to make them bimorph piezoelectric energy harvesters. The unit cell presented in the figure has only 4 cantilevers, but more cantilevers could be considered at each node. In later sections, cantilevers are called resonators.

Figure 2.3 shows the 6 types of unit cells used in later sections. Types I and IV have horizontal, vertical, 45° and 135° symmetries, where type I has only one cantilever at each

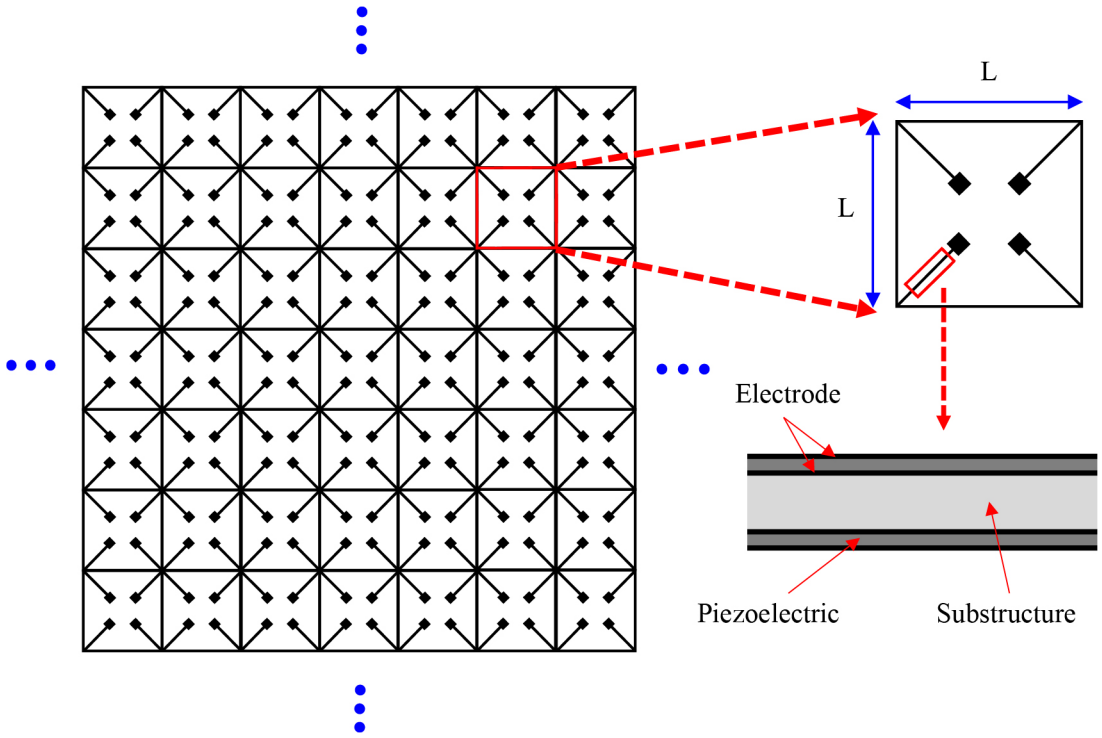

Figure 2.2: Infinite 2D panel built from a square unit cell with cantilevers in its corners, which have 2 layers of piezoelectric attached, which transforms them into bimorph energy harvesters.

node, while type IV has 2. Given the symmetries that must be met, all the cantilevers must have the same physical and geometric properties. Types II and V have no internal symmetries, with the particularity that in type II all cantilevers must have the same physical and geometric properties, but they can be at different angles, and in type V the physical and geometric properties of the two cantilevers of a node can be defined independently, but the other 3 nodes must have the same 2 cantilevers (may be at different angles). In cases III and VI there are no internal symmetries either, and in this case each cantilever can be defined independently, so type III accepts 4 different cantilevers and type VI accepts 8.

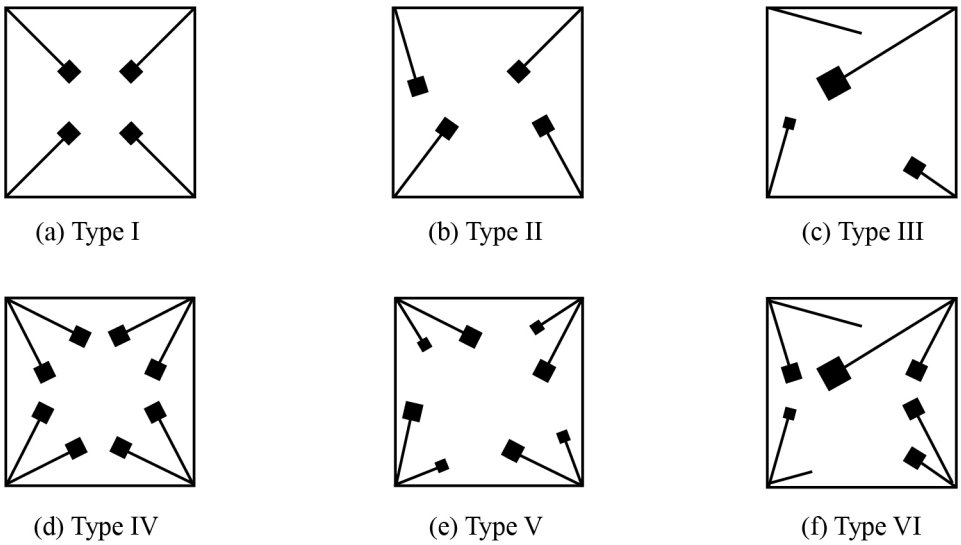

(a) Type I (b) Type II (c) Type III

(d) Type IV (e) Type V (f) Type VI

Figure 2.3: Square unit cells with resonators at their nodes. These are grouped into 6 types, type I, II and III correspond to cells with 1 resonator in each node, in which **(a)** type I comply with horizontal, vertical and oblique symmetries, **(b)** type II does not present symmetry axes but all the resonators must have the same physical and geometric properties, and **(c)** type III do not have symmetries and the resonators can have different properties. On the other hand, type IV, V and VI unit cells have 2 resonators at each node, **(d)** type IV must be symmetrical just like type I, **(e)** type V do not have symmetries but only 2 different resonators can be defined since all the nodes must have the same 2 resonators, and the **(f)** type VI do not present any requirement on the resonators.

Chapter 3

Numerical Model and Validation

The studied metamaterials are built by adopting a finite element approach. The resonators have piezoelectric layers attached, so an electromechanically coupled model must be developed. This section details the development of the model and also presents its validation and comparison with what is found in the literature.

3.1. Generalized Hamilton's principle for a piezoelectric energy harvester

In the absence of magnetic effects and for a set of discrete mechanical forces $\mathbf{f}$ applied at locations (x_i, y_i) and for a set of discrete electric charge outputs q extracted at locations (x_j, y_j), the generalized Hamilton's principle for an electroelastic body is [52]:

$$\begin{aligned}\int_{t_1}^{t_2} \Bigg[\int_{V_s} \rho_s \delta\dot{\mathbf{u}}^t \dot{\mathbf{u}}\, dV_s + \int_{V_p} \rho_p \delta\dot{\mathbf{u}}^t \dot{\mathbf{u}}\, dV_p - \int_{V_s} \delta\mathbf{S}^t \mathbf{c}_s \mathbf{S}\, dV_s - \int_{V_p} \delta\mathbf{S}^t \mathbf{c}_p^E \mathbf{S}\, dV_p \\ + \int_{V_p} \delta\mathbf{S}^t \mathbf{e}^t \mathbf{E}\, dV_p + \int_{V_p} \delta\mathbf{E}^t \mathbf{e}\mathbf{S}\, dV_p + \int_{V_p} \delta\mathbf{E}^t \varepsilon^s \mathbf{E}\, dV_p + \sum_{i=1}^{n_f} \delta\mathbf{u}(x_i, y_i, t) \cdot \mathbf{f}(x_i, y_i, t) \\ + \sum_{j=1}^{n_q} \delta\varphi(x_j, y_j, t) q(x_j, y_j, t) dt = 0\end{aligned} \tag{3.1}$$

where $\mathbf{u}$ is the vector of mechanical displacements, $\mathbf{S}$ is the vector of mechanical strain components, $\mathbf{E}$ is the vector of electric field components, ρ is the mass density, V is the volume, $\mathbf{c}$ is the elastic stiffness matrix, $\mathbf{e}$ is the matrix of piezoelectric constants, ε is the matrix of permittivity components, n_f is the number of discrete mechanical forces, φ is the scalar electrical potential and n_q is the number of discrete electrode pairs, t denotes transpose when it is used as a superscript (otherwise it stands for the time) and an over-dot represents differentiation with respect to time. Subscripts s and p stand for the substructure and piezocelectric layers, respectively, and superscript E and S denote that the parameters are measured at constant electric field and constant strain, respectively.

3.2. Finite Element Model for Piezoelectric Beams

The structural model is built by adopting a finite element approach. The models are composed entirely of one-dimensional elements, which are modeled using Bernoulli beams with two nodes per element and three degrees of freedom per node (one rotation and two displacements), as shown in figure 3.1, where L_e corresponds to the length of the element.

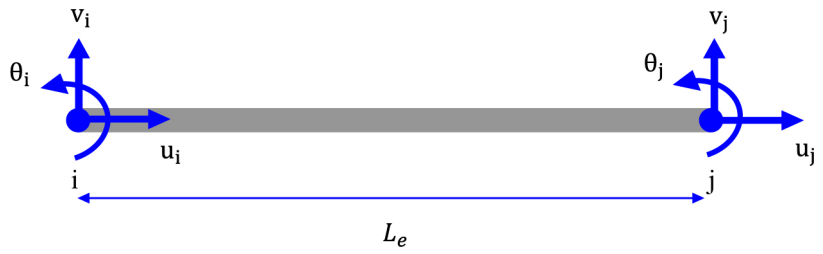

Figure 3.1: 2D Euler-Bernoulli beam element of length L_e, with two nodes per element and three degrees of freedom per node.

In many cases, in finite element development, it is convenient to use "Natural coordinates", which are dimensionless coordinates that facilitate the process of obtaining the interpolation functions and allow to use curved sides or faces in the elements in the flat or three-dimensional case, transforming the geometry to a simplified situation. Figure 3.2 shows two schemes of a Bernoulli beam with the reference system in Cartesian and Natural coordinates, locating in both cases the reference system in the center of the element.

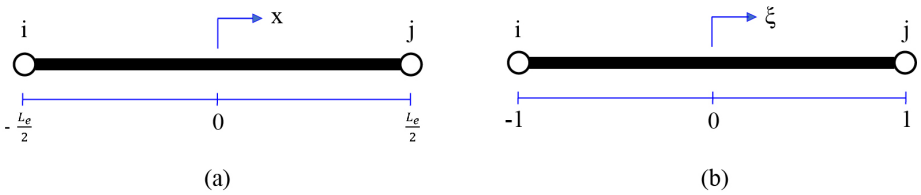

Figure 3.2: Bernoulli beam with nodes i and j and its local reference system located at the center of the element in **(a)** Cartesian and **(b)** Natural coordinates.

The position of any point within the element expressed in Cartesian coordinates is the following:

$$x^e_{(x)} = \begin{bmatrix} N_{1(x)} & N_{2(x)} \end{bmatrix} \begin{bmatrix} x^e_1 \\ x^e_2 \end{bmatrix} = \mathbf{N}_{(x)}\mathbf{x}^e \tag{3.2}$$

where $N_{1(x)} = \frac{1}{2} - \frac{x}{L_e}$ and $N_{2(x)} = \frac{1}{2} + \frac{x}{L_e}$ are the shape functions in Cartesian coordinates.

In the case of Natural coordinates, the position of any point within the element is the following:

$$x^e_{(\xi)} = \begin{bmatrix} N_{1(\xi)} & N_{2(\xi)} \end{bmatrix} \begin{bmatrix} x^e_1 \\ x^e_2 \end{bmatrix} = \mathbf{N}_{(\xi)} \mathbf{x}^e \tag{3.3}$$

where $N_{1(\xi)} = \frac{1}{2} - \frac{\xi}{2}$ and $N_{2(\xi)} = \frac{1}{2} + \frac{\xi}{2}$ are the shape functions in Natural coordinates.

Since the two parameterizations must be consistent, it must be satisfied that $\frac{x}{L_e} = \frac{\xi}{2}$, which implies that $\frac{\partial \xi}{\partial x} = \frac{2}{L_e}$.

The displacement in the axial direction associated with the tension of the bar ($u^e_{a(\xi,t)}$) responds to a first-order differential equation, so interpolation functions of type C^0 are required, which means that the same functions used to define the geometry of the element ($N_{1(\xi)}$ and $N_{2(\xi)}$) can be used for the axial displacement. Given this, the displacement is determined as follows:

$$u^e_{a(\xi,t)} = \begin{bmatrix} N_{1(\xi)} & N_{2(\xi)} \end{bmatrix} \begin{bmatrix} u^e_{1(t)} \\ u^e_{2(t)} \end{bmatrix} = \mathbf{N}_{(\xi)} \mathbf{q}^e_{1(t)} \tag{3.4}$$

For the bending problem, continuity is needed in the deflection and in its derivative (rotation), so it is a problem of 4 variables (2 deflections and 2 rotations), this implies that a cubic approximation of deflection is needed. The deflection ($v^e_{(\xi,t)}$) and rotation ($\theta^e_{(\xi,t)}$) are determined with the following equations:

$$v^e_{(\xi,t)} = a_{(t)} + b_{(t)}\xi + c_{(t)}\xi^2 + d_{(t)}\xi^3 \tag{3.5}$$

$$\theta^e_{(\xi,t)} = \frac{\mathrm{d}v_{(\xi,t)}}{\mathrm{d}x} = \frac{\mathrm{d}v_{(\xi,t)}}{\mathrm{d}\xi}\frac{\mathrm{d}\xi}{\mathrm{d}x} = \left(b_{(t)} + 2c_{(t)}\xi + 3d_{(t)}\xi^2\right)\frac{2}{L_e} \tag{3.6}$$

where a, b, c and d are time-dependent coefficients to be determined as a function of nodal deflections and rotations $v^e_{1(t)}$, $\theta^e_{1(t)}$, $v^e_{2(t)}$ and $\theta^e_{2(t)}$. For this, the equations 3.5 and 3.6 must be evaluated at the ends of the beam ($\xi = -1$ and $\xi = 1$), which generates the following system of equations:

$$\begin{aligned} v^e_{1(t)} &= v^e_{(\xi=-1,t)} = a_{(t)} - b_{(t)} + c_{(t)} - d_{(t)} \\ \theta^e_{1(t)} &= \theta^e_{(\xi=-1,t)} = (b_{(t)} - 2c_{(t)} + 3d_{(t)})\frac{2}{L_e} \\ v^e_{2(t)} &= v^e_{(\xi=1,t)} = a_{(t)} + b_{(t)} + c_{(t)} + d_{(t)} \\ \theta^e_{2(t)} &= \theta^e_{(\xi=1,t)} = (b_{(t)} + 2c_{(t)} + 3d_{(t)})\frac{2}{L_e} \end{aligned} \tag{3.7}$$

If the value of the coefficients a, b, c and d are solved as a function of the nodal displacements and rotations, and this is replaced in the equation 3.5 and 3.6, the following expressions are obtained for $v^e_{(\xi,t)}$ and $\theta^e_{(\xi,t)}$:

$$v^e_{(\xi,t)} = \begin{bmatrix} H_{1(\xi)} & \frac{L_e}{2}H_{2(\xi)} & H_{3(\xi)} & \frac{L_e}{2}H_{4(\xi)} \end{bmatrix} \begin{bmatrix} v^e_{1(t)} \\ \theta^e_{1(t)} \\ v^e_{2(t)} \\ \theta^e_{2(t)} \end{bmatrix} = \mathbf{H}_{(\xi)}\mathbf{q}^e_{2(t)} \tag{3.8}$$

$$\theta^e_{(\xi,t)} = \frac{2}{L_e} \begin{bmatrix} H'_{1(\xi)} & \frac{L_e}{2}H'_{2(\xi)} & H'_{3(\xi)} & \frac{L_e}{2}H'_{4(\xi)} \end{bmatrix} \begin{bmatrix} v^e_{1(t)} \\ \theta^e_{1(t)} \\ v^e_{2(t)} \\ \theta^e_{2(t)} \end{bmatrix} = \frac{2}{L_e}\mathbf{H}'_{(\xi)}\mathbf{q}^e_{2(t)} \tag{3.9}$$

where $\mathbf{q}^e_{2(t)}$ is a vector that has the vertical displacement and rotations at the nodes, and the $H_{i(\xi)}$ and their derivatives (for i = 1, 2, 3 and 4) are the shape functions, and are given by the following expressions:

$$\begin{aligned}
H_{1(\xi)} &= \frac{1}{4}(2 - 3\xi + \xi^3) & H'_{1(\xi)} &= \frac{1}{4}(-3 + 3\xi^2) & H''_{1(\xi)} &= \frac{1}{4}(6\xi) \\
H_{2(\xi)} &= \frac{1}{4}(1 - \xi - \xi^2 + \xi^3) & H'_{2(\xi)} &= \frac{1}{4}(-1 - 2\xi + 3\xi^2) & H''_{2(\xi)} &= \frac{1}{4}(-2 + 6\xi) \\
H_{3(\xi)} &= \frac{1}{4}(2 + 3\xi - \xi^3) & H'_{3(\xi)} &= \frac{1}{4}(3 - 3\xi^2) & H''_{3(\xi)} &= \frac{1}{4}(-6\xi) \\
H_{4(\xi)} &= \frac{1}{4}(-1 - \xi + \xi^2 + \xi^3) & H'_{4(\xi)} &= \frac{1}{4}(-1 + 2\xi + 3\xi^2) & H''_{4(\xi)} &= \frac{1}{4}(2 + 6\xi)
\end{aligned} \tag{3.10}$$

The equations 3.4 and 3.8 can be joined to obtain a system of equations for displacements along the beam in terms of the nodal displacements and rotations:

$$\begin{bmatrix} u^e_{a(\xi,t)} \\ v^e_{(\xi,t)} \end{bmatrix} = \begin{bmatrix} N_{1(\xi)} & 0 & 0 & N_{2(\xi)} & 0 & 0 \\ 0 & H_{1(\xi)} & \frac{L_e}{2}H_{2(\xi)} & 0 & H_{3(\xi)} & \frac{L_e}{2}H_{4(\xi)} \end{bmatrix} \begin{bmatrix} u^e_{1(t)} \\ v^e_{1(t)} \\ \theta^e_{1(t)} \\ u^e_{2(t)} \\ v^e_{2(t)} \\ \theta^e_{2(t)} \end{bmatrix} = \mathbf{\Gamma}_{(\xi)}\mathbf{q}^e_{(t)} \tag{3.11}$$

The derivative with respect to time of equation 3.11 only requires obtaining the derivative of the nodal values and the same shape functions $\mathbf{\Gamma}_{(\xi)}$ are used because these do not depend on time, so the expression for the derivative is the following:

$$\begin{bmatrix} \dot{u}^e_{a(\xi,t)} \\ \dot{v}^e_{(\xi,t)} \end{bmatrix} = \mathbf{\Gamma}_{(\xi)}\dot{\mathbf{q}}^e_{(t)} \tag{3.12}$$

The displacement in the axial direction of a point $(u^e_{f(\xi,t)})$ in the cross section at a distance "y" from the neutral axis, considering small deformations, can be calculated by the following

expression:

$$u^e_{f(\xi,t)} = -y\theta^e_{(\xi,t)} = \frac{-2y}{L_e}\mathbf{H}'_{(\xi)}\mathbf{q}^e_{2(t)} \tag{3.13}$$

where $\theta^e_{(\xi,t)}$ was obtained by the equation 3.9.

The total displacement in the axial direction ($u^e_{(\xi,t)}$) can be calculated as the sum of $u^e_{a(\xi,t)}$ and $u^e_{f(\xi,t)}$ (equations 3.4 and 3.13). Based on this, and applying the chain rule, the axial deformation is expressed by the following expression:

$$\begin{aligned}\varepsilon^e &= \frac{\partial u^e_{(\xi,t)}}{\partial x} = \frac{\partial u^e_{a(\xi,t)}}{\partial \xi}\frac{\partial \xi}{\partial x} + \frac{\partial u^e_{f(\xi,t)}}{\partial \xi}\frac{\partial \xi}{\partial x} \\ &= \frac{2}{L_e}\mathbf{N}'_{(\xi)}\mathbf{q}^e_{1(t)} - y\frac{4}{L_e^2}\mathbf{H}''_{(\xi)}\mathbf{q}^e_{2(t)} \\ &= \mathbf{B}_{(\xi)}\mathbf{q}^e_{(t)}\end{aligned} \tag{3.14}$$

where $\mathbf{B}_{(\xi)}$ is defined in terms of the shape functions, and corresponds to the following vector:

$$\mathbf{B}_{(\xi)} = \left[\frac{2}{L_e}N'_{1(\xi)} \quad \frac{-4y}{L_e^2}H''_{1(\xi)} \quad \frac{-2y}{L_e}H''_{2(\xi)} \quad \frac{2}{L_e}N'_{2(\xi)} \quad \frac{-4y}{L_e^2}H''_{3(\xi)} \quad \frac{-2y}{L_e}H''_{4(\xi)}\right] \tag{3.15}$$

To obtain the elementary stresses ($\mathbf{S}$), the deformation of equation 3.15 is used in a linear elastic constitutive law with proportionality constant c_s as follows:

$$\mathbf{S} = c_s\varepsilon^e = c_s\mathbf{B}_{(\xi)}\mathbf{q}^e_{(t)} \tag{3.16}$$

Due to the geometry of the beams and cantilevers (rectangular cross section), the piezoelectric layer is poled in the thickness direction (y-direction), so the non-zero electric field component E (which is assumed to be uniform) can be calculated by the following equation:

$$E = -\frac{\partial \varphi}{\partial y} = -\frac{v_p}{h_p} = -B_E v_p \tag{3.17}$$

where h_p is the thickness of the piezoelectric layer.

Based on the Hamilton's principle given by equation 3.1, and using the equations 3.12, 3.16 and 3.17 for the mechanical velocity, the mechanical strain and the electric field, the element mass matrix in local coordinates ($\mathbf{m}_l$), stiffness matrix ($\mathbf{k}_l$), electromechanical coupling vector ($\mathbf{\Theta}$) and capacitance (c_p) can be calculated by the following integrals:

$$\mathbf{m}_l = \int_{V_s} \rho_s \mathbf{\Gamma}^t \mathbf{\Gamma} \; dV_s + \int_{V_p} \rho_p \mathbf{\Gamma}^t \mathbf{\Gamma} \; dV_p \tag{3.18}$$

$$\mathbf{k}_l = \int_{V_s} \mathbf{B}^t c_s \mathbf{B} \; dV_s + \int_{V_p} \mathbf{B}^t c_p^E \mathbf{B} \; dV_p \tag{3.19}$$

$$\mathbf{\Theta} = \beta \int_{V_p} \mathbf{B}^t e_{31} B_E \; dV_p \tag{3.20}$$

$$c_p = \alpha \int_{V_p} B_E \varepsilon_{33}^S B_E \; dV_p \tag{3.21}$$

where α and β are constants that depend on whether the piezoelectric harvester is unimorph or bimorph and are explained later, and only the e_{31} and ε_{33}^S components are considered because the piezoelectric layer is poled in the thickness direction. The volume differentials can be expressed as:

$$\begin{aligned} dV_s &= dAdx = \frac{L_e}{2} dAd\xi \\ dV_p &= dAdx = \frac{L_e}{2} dAd\xi \end{aligned} \tag{3.22}$$

If the integrals above are developed, the following results are obtained:

$$\mathbf{m}_l = \frac{L_e}{420}(\rho_s A_s + \rho_p A_p) \begin{bmatrix} 140 & 0 & 0 & 70 & 0 & 0 \\ 0 & 156 & 22L_e & 0 & 54 & -13L_e \\ 0 & 22L_e & 4L_e^2 & 0 & 13L_e & -3L_e^2 \\ 70 & 0 & 0 & 140 & 0 & 0 \\ 0 & 54 & 13L_e & 0 & 156 & -22L_e \\ 0 & -13L_e & -3L_e^2 & 0 & -22L_e & 4L_e^2 \end{bmatrix} \tag{3.23}$$

$$\mathbf{k}_l = \begin{bmatrix} \frac{Y_s A_s + Y_p A_p}{L_e} & 0 & 0 & -\frac{Y_s A_s + Y_p A_p}{L_e} & 0 & 0 \\ 0 & \frac{12(Y_s I_s + Y_p I_p)}{L_e^3} & \frac{6(Y_s I_s + Y_p I_p)}{L_e^2} & 0 & -\frac{12(Y_s I_s + Y_p I_p)}{L_e^3} & \frac{6(Y_s I_s + Y_p I_p)}{L_e^2} \\ 0 & \frac{6(Y_s I_s + Y_p I_p)}{L_e^2} & \frac{4(Y_s I_s + Y_p I_p)}{L_e} & 0 & -\frac{6(Y_s I_s + Y_p I_p)}{L_e^2} & \frac{2(Y_s I_s + Y_p I_p)}{L_e} \\ -\frac{Y_s A_s + Y_p A_p}{L_e} & 0 & 0 & \frac{Y_s A_s + Y_p A_p}{L_e} & 0 & 0 \\ 0 & -\frac{12(Y_s I_s + Y_p I_p)}{L_e^3} & -\frac{6(Y_s I_s + Y_p I_p)}{L_e^2} & 0 & \frac{12(Y_s I_s + Y_p I_p)}{L_e^3} & -\frac{6(Y_s I_s + Y_p I_p)}{L_e^2} \\ 0 & \frac{6(Y_s I_s + Y_p I_p)}{L_e^2} & \frac{2(Y_s I_s + Y_p I_p)}{L_e} & 0 & -\frac{6(Y_s I_s + Y_p I_p)}{L_e^2} & \frac{12(Y_s I_s + Y_p I_p)}{L_e^3} \end{bmatrix} \tag{3.24}$$

$$\mathbf{\Theta} = \beta \frac{e_{31} b}{2} (h_p + h_s) \begin{bmatrix} 0 \\ 0 \\ 1 \\ 0 \\ 0 \\ -1 \end{bmatrix} \tag{3.25}$$

$$c_p = \alpha \frac{\varepsilon_{33} b L_e}{h_p} \tag{3.26}$$

where b, h, I, A, Y are the width, thickness, moment of inertia, area and Young's modulus, respectively (the elastic stiffness c_s and c_p^E are replaced by Y_s and Y_p, respectively). Subscripts s and p stand for the substructure and piezocelectric layers, respectively.

If a unimorph piezoelectric energy harvester is considered, only one layer of piezoelectric must be considered in the calculation of the mass and stiffness matrices, and additionally $\alpha = \beta = 1$ must be used in equations 3.20 and 3.21. On the other hand, if a bimorph harvester is considered, the mass and stiffness must consider the presence of the two piezoelectric layers (which mainly affects the calculation of A_p and I_p), and the value of the coefficients α and β depends on the way the two piezoelectric layers are connected to the external electrical load. For parallel connection (larger current), the two layers are poled in the same direction and $\alpha = \beta = 2$, for the series connection (larger voltage), the two layers are poled in the opposite direction and $\alpha = 1/2$ and $\beta = 1$.

Tip masses at the ends of the cantilevers (as shown in figure 2.3), are modeled as undeformable point masses. To add them in the elementary matrices, the value of the tip mass must be added in the components $\mathbf{m}_l$[1,1] and $\mathbf{m}_l$[2,2] if the mass is added in node i, and in the components $\mathbf{m}_l$[4,4] and $\mathbf{m}_l$[5,5] if the mass is added at node j (see figure 3.1).

The mass and stiffness matrices (equations 3.23 and 3.24) should be referred to the same global coordinate system. For this reason, the local matrices of each element must be transformed using the matrix R presented in equation 3.27), whose function is to carry a matrix of local to global coordinates, or vice versa. The angle ϕ in the equation corresponds to the inclination of the element with respect to the horizontal axis of the global coordinate system, measured counterclockwise. Equations 3.28 and 3.29 present the transformation from local to global coordinates of the mass and stiffness matrices, respectively.

$$\mathbf{R} = \begin{bmatrix} cos(\phi) & sin(\phi) & 0 & 0 & 0 & 0 \\ -sin(\phi) & cos(\phi) & 0 & 0 & 0 & 0 \\ 0 & 0 & 1 & 0 & 0 & 0 \\ 0 & 0 & 0 & cos(\phi) & sin(\phi) & 0 \\ 0 & 0 & 0 & -sin(\phi) & cos(\phi) & 0 \\ 0 & 0 & 0 & 0 & 0 & 1 \end{bmatrix} \tag{3.27}$$

$$\mathbf{k}_g = \mathbf{R}^t \mathbf{k}_l \mathbf{R} \tag{3.28}$$

$$\mathbf{m}_g = \mathbf{R}^t \mathbf{m}_l \mathbf{R} \tag{3.29}$$

After changing from local to global coordinates the elementary matrices, they must be assembled (add the components of various elements that concur in the same node) to obtain the global equations of motion, which are the following:

$$\mathbf{M}\ddot{\mathbf{\Psi}} + \mathbf{C}\dot{\mathbf{\Psi}} + \mathbf{K}\mathbf{\Psi} - \mathbf{\Theta}\mathbf{v} = \mathbf{f} \tag{3.30}$$

$$\mathbf{C_p}\mathbf{v} + \mathbf{Q} + \mathbf{\Theta}^t\dot{\mathbf{\Psi}} = \mathbf{0} \tag{3.31}$$

where $\mathbf{M}$ is the global mass matrix (n_m x n_m), $\mathbf{K}$ is the global stiffness matrix (n_m x n_m), $\mathbf{C}$ is the global mechanical damping matrix (n_m x n_m), $\mathbf{\Theta}$ is the global electromechanical coupling matrix (n_m x n_e), $\mathbf{C_p}$ is the global capacitance matrix (n_e x n_e), $\mathbf{F}$ is the global vector of mechanical forces (n_m x 1), $\mathbf{Q}$ is the global vector of electric charge outputs (n_m x 1), $\mathbf{\Psi}$ is the global vector of nodal displacements and rotations (n_m x 1) and $\mathbf{v}$ is the global vector of voltage outputs (n_e x 1). The coefficients n_m and n_e are the number of degrees of freedom and the number of elements of the structure, respectively. The global mechanical damping matrix is assumed to be proportional to the mass and stiffness matrices:

$$\mathbf{C} = \gamma_1\mathbf{M} + \gamma_2\mathbf{K} \tag{3.32}$$

where γ_1 and γ_2 are the constants of proportionality.

Piezoelectric layers come from the manufacturer with thin and very conductive electrode layers on the top and bottom surfaces. It is therefore reasonable to assume that all finite elements that correspond to the same beam generate the same voltage output. For example, if beam i is discretized in n_i elements, it is true that $v_1^i = ... = v_k^i = ... = v_{n_i}^i = v_p^i \quad \forall\, i \in [1, N_b]$, where v_k^i indicates the voltage output of the element k of the beam i, and N_b is the total number of beams in the structure, such that $\sum_{i=1}^{N_b} n_i = n_e$. If these considerations are applied, the voltage vector ($\mathbf{v}$) can be simplified as follows:

$$\mathbf{v} = \begin{bmatrix} \begin{bmatrix} v_1^1 \\ \vdots \\ v_{n_1}^1 \end{bmatrix} \\ \vdots \\ \begin{bmatrix} v_1^i \\ \vdots \\ v_{n_i}^i \end{bmatrix} \\ \vdots \\ \begin{bmatrix} v_1^{N_b} \\ \vdots \\ v_{n_{N_b}}^{N_b} \end{bmatrix} \end{bmatrix} = \begin{bmatrix} \mathbf{r}_{n_1 x 1} \cdot v_p^1 \\ \vdots \\ \mathbf{r}_{n_i x 1} \cdot v_p^i \\ \vdots \\ \mathbf{r}_{n_{N_b} x 1} \cdot v_p^{N_b} \end{bmatrix} = \begin{bmatrix} \mathbf{r}_{n_1 x 1} & \mathbf{0} & \mathbf{0} & \mathbf{0} & \mathbf{0} \\ \mathbf{0} & \ddots & \mathbf{0} & \mathbf{0} & \mathbf{0} \\ \mathbf{0} & \mathbf{0} & \mathbf{r}_{n_k x 1} & \mathbf{0} & \mathbf{0} \\ \mathbf{0} & \mathbf{0} & \mathbf{0} & \ddots & \mathbf{0} \\ \mathbf{0} & \mathbf{0} & \mathbf{0} & \mathbf{0} & \mathbf{r}_{n_{N_b} x 1} \end{bmatrix} \begin{bmatrix} v_p^1 \\ \vdots \\ v_p^i \\ \vdots \\ v_p^{N_b} \end{bmatrix} = \mathbf{I}\mathbf{v_p} \tag{3.33}$$

where $\mathbf{r}$ is a vector of ones with the dimension indicated in the subscript, $\mathbf{v_p}$ contains the voltages of each piezoelectric beam (N_bx1), and the $\mathbf{I}$ matrix (n_exN_b) is the one that relates the voltage vector ($\mathbf{v}$) with the reduced voltage vector ($\mathbf{v_p}$).

Taking the time derivative of equation 3.31 and pre-multiplying by the (n_exN_b) matrix $\mathbf{I}^t$, one can obtain the following equation:

$$\mathbf{I}^t\mathbf{C_p}\dot{\mathbf{v}} + \mathbf{I}^t\dot{\mathbf{Q}} + \mathbf{I}^t\mathbf{\Theta}^t\dot{\mathbf{\Psi}} = \mathbf{0} \tag{3.34}$$

If equation 3.33 is replaced in equation 3.34, the following equation is obtained:

$$\mathbf{I}^t\mathbf{C_p}\mathbf{I}\dot{\mathbf{v}}_\mathbf{p} + \mathbf{I}^t\mathbf{R}\mathbf{I}\mathbf{v_p} + \mathbf{I}^t\mathbf{\Theta}^t\dot{\mathbf{\Psi}} = \mathbf{0} \tag{3.35}$$

If the variable changes are made $\tilde{\mathbf{C}}_\mathbf{p} = \mathbf{I}^t\mathbf{C_p}\mathbf{I}$, $\tilde{\mathbf{R}} = \mathbf{I}^t\mathbf{R}\mathbf{I}$ and $\tilde{\mathbf{\Theta}} = \mathbf{\Theta}\mathbf{I}$, the following equations of motion are obtained:

$$\mathbf{M}\ddot{\mathbf{\Psi}} + \mathbf{C}\dot{\mathbf{\Psi}} + \mathbf{K}\mathbf{\Psi} - \tilde{\mathbf{\Theta}}\mathbf{v_p} = \mathbf{f} \tag{3.36}$$

$$\tilde{\mathbf{C}}_\mathbf{p}\dot{\mathbf{v}}_\mathbf{p} + \tilde{\mathbf{R}}\mathbf{v_p} + \tilde{\mathbf{\Theta}}^t\dot{\mathbf{\Psi}} = \mathbf{0} \tag{3.37}$$

which are the governing electromechanical equations.

If the structure is subjected to harmonic displacements at the base, the voltage and relative tip motion output to base acceleration FRF can be obtained from equations 3.36 and 3.37:

$$\frac{\mathbf{v_p}}{-\omega^2 Y_0 e^{j\omega t}} = j\omega \left(\tilde{\mathbf{R}} + j\omega\tilde{\mathbf{C}}_\mathbf{p}\right)^{-1} \tilde{\mathbf{\Theta}}^T \left(-\omega^2\mathbf{M} + j\omega\mathbf{C} + \mathbf{K} + j\omega \left(\tilde{\mathbf{R}} + j\omega\tilde{\mathbf{C}}_\mathbf{p}\right)^{-1} \tilde{\mathbf{\Theta}}\tilde{\mathbf{\Theta}}^t\right)^{-1} \mathbf{m}^* \tag{3.38}$$

$$\frac{\mathbf{w_{rel}}}{-\omega^2 Y_0 e^{j\omega t}} = -\left(-\omega^2\mathbf{M} + j\omega\mathbf{C} + \mathbf{K} + j\omega \left(\tilde{\mathbf{R}} + j\omega\tilde{\mathbf{C}}_\mathbf{p}\right)^{-1} \tilde{\mathbf{\Theta}}\tilde{\mathbf{\Theta}}^t\right)^{-1} \mathbf{m}^* \tag{3.39}$$

where **m*** is an (n_m x 1) mass vector obtained from the global forcing term **f** for the base excitation problem.

3.3. State space formulation

If the variable $\mathbf{z} = \begin{bmatrix}\mathbf{\Psi} & \dot{\mathbf{\Psi}} & \mathbf{v_p}\end{bmatrix}^t$ is replaced in the equation 3.36 and 3.37, we get the following expression for $\dot{\mathbf{z}}$:

$$\dot{\mathbf{z}} = \overbrace{\begin{bmatrix} \mathbf{0} & \mathbf{I} & \mathbf{0} \\ -\mathbf{M}^{-1}\mathbf{K} & -\mathbf{M}^{-1}\mathbf{C} & \mathbf{M}^{-1}\tilde{\mathbf{\Theta}} \\ \mathbf{0} & -\tilde{\mathbf{C}}_\mathbf{p}^{-1}\tilde{\mathbf{\Theta}}^t & -\tilde{\mathbf{C}}_\mathbf{p}^{-1}\tilde{\mathbf{R}} \end{bmatrix}}^{\mathbf{A}} \mathbf{z} + \overbrace{\begin{bmatrix}\mathbf{0}\\ \mathbf{f}\\ \mathbf{0}\end{bmatrix}}^{\mathbf{b}} \tag{3.40}$$

The natural frequencies can be obtained by solving the eigenvalue problem associated with matrix **A**.

3.4. Bloch theorem

The development presented in the previous sections is valid for any structure, which is very useful for working with finite arrangements (for example, the panels of section 7). In case it is required to work with the unit cell of an infinite periodic structure, the Floquet–Bloch periodic condition must be applied.

From the direct lattice, it is possible to build a secondary lattice called reciprocal lattice, which is useful to study the physical phenomena of wave behavior. Like the direct lattice, the reciprocal one can also be completely constructed by basis vectors that are denoted $\mathbf{e^j}$ (j = 1, 2 for two-dimensional case), and must comply with the same properties of the direct lattice. The reciprocal lattice vectors can be calculated from the direct lattice vectors using the following relationship:

$$\mathbf{e_i} \cdot \mathbf{e^j} = 2\pi\delta_{ij} \tag{3.41}$$

where δ_{ij} is the Kronecker delta, so $\delta_{ij} = 1$ for $i = j$ and $\delta_{ij} = 0$ otherwise, and $\mathbf{e_i}$ (i = 1, 2) are the direct lattice vectors.

Figure 3.3a shows 9 nodes of a square direct lattice with periodicity A, and figure 3.3b shows 9 points of the associated reciprocal lattice, which has a periodicity of $\frac{2\pi}{A}$. The gray square of the reciprocal lattice corresponds to the first Brillouin zone (BZ), and the wave vectors that belong to the vertices, the middle of the sides and the center are indicated (N, Y, M, X, $\overline{O}$, $\overline{Y}$, $\overline{M}$, $\overline{X}$ and Γ).

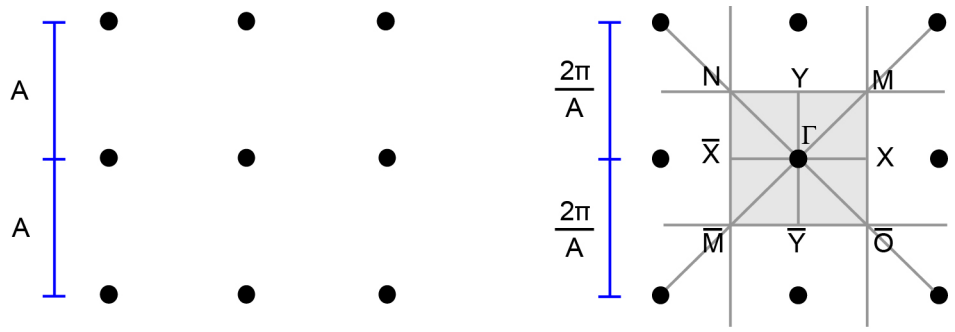

(a) (b)

Figure 3.3: **(a)** Extract of a square direct lattice of periodicity A, and its **(b)** reciprocal lattice of periodicity $\frac{2\pi}{A}$. The Brillouin Zone is indicated in gray, and the main wave vectors are detailed (N, Y, M, X, $\overline{O}$, $\overline{Y}$, $\overline{M}$, $\overline{X}$ and Γ).

The wavelength and direction of wave propagation is described by the wave vector. Any point $\mathbf{k}$ from the reciprocal space (not necessarily belonging the lattice) represents a flat wave with wave vector $\mathbf{k}$, this is why the reciprocal lattice is scaled by 2π in equation 3.41, so that the coordinates of the wave vector can be expressed with the same vector base of the reciprocal lattice. In this way, a generic wave vector $\mathbf{k}$ can be written as follows:

$$\mathbf{k} = k_1\mathbf{e^1} + k_2\mathbf{e^2}$$

where k_1 and k_2 are real numbers.

According to the Floquet–Bloch wave theory, the displacement ($\mathbf{u}$) for a periodic unit cell satisfies the following relationship:

$$\mathbf{u}(\mathbf{x}+\mathbf{r}) = \mathbf{u}(\mathbf{x})e^{i\mathbf{kr}} \tag{3.42}$$

where $i^2 = -1$, $\mathbf{k}$ is the wave vector, $\mathbf{r}$ is the cell periodicity and $\mathbf{x}$ is a position within the periodic array.

In figure 3.3 a generic square unit cell is presented, where $\mathbf{\Psi_{BL}}$, $\mathbf{\Psi_L}$, $\mathbf{\Psi_{TL}}$, $\mathbf{\Psi_T}$, $\mathbf{\Psi_{TR}}$, $\mathbf{\Psi_R}$, $\mathbf{\Psi_{BR}}$, $\mathbf{\Psi_B}$ are the points that lie on the edge of the unit cell, where the subscripts T, B, L and R stand for top, bottom, left and right, respectively. Also, the points inside the unit cell are represented by $\mathbf{\Psi_I}$. It is important to highlight that only the points that are in the corners (those with 2 subscripts) are unique points, while the nomenclature that represents the other points refers to sets of points (there can be several internal points $\mathbf{\Psi_I}$, several points in the left side $\mathbf{\Psi_L}$, etc). The figure also shows the direct lattice vectors $\mathbf{e_1}$ and $\mathbf{e_2}$.

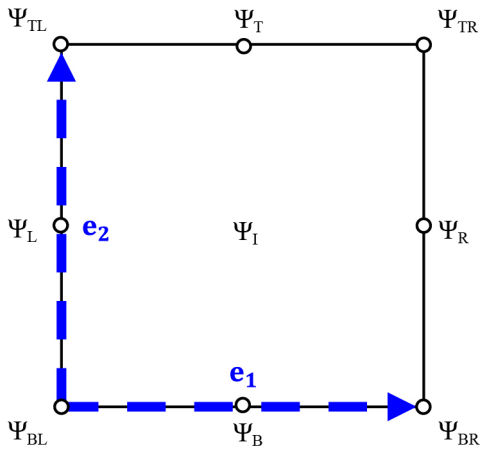

Figure 3.4: Representation of a 2D square unit cell, grouping its components into $\mathbf{\Psi_{BL}}$, $\mathbf{\Psi_L}$, $\mathbf{\Psi_{TL}}$, $\mathbf{\Psi_T}$, $\mathbf{\Psi_{TR}}$, $\mathbf{\Psi_R}$, $\mathbf{\Psi_{BR}}$, $\mathbf{\Psi_B}$.

Applying equation 3.42 in the configuration presented in figure 3.4, the matrix system indicated in equation 3.43 is obtained.

$$\overbrace{\begin{bmatrix}\mathbf{\Psi_L}\\ \mathbf{\Psi_R}\\ \mathbf{\Psi_B}\\ \mathbf{\Psi_T}\\ \mathbf{\Psi_{BL}}\\ \mathbf{\Psi_{BR}}\\ \mathbf{\Psi_{TL}}\\ \mathbf{\Psi_{TR}}\\ \mathbf{\Psi_I}\end{bmatrix}}^{\mathbf{\Psi}} = \overbrace{\begin{bmatrix}\mathbf{I} & \mathbf{0} & \mathbf{0} & \mathbf{0}\\ \mathbf{I}e^{i\mathbf{k}\cdot\mathbf{e_1}} & \mathbf{0} & \mathbf{0} & \mathbf{0}\\ \mathbf{0} & \mathbf{I} & \mathbf{0} & \mathbf{0}\\ \mathbf{0} & \mathbf{I}e^{i\mathbf{k}\cdot\mathbf{e_2}} & \mathbf{0} & \mathbf{0}\\ \mathbf{0} & \mathbf{0} & \mathbf{I} & \mathbf{0}\\ \mathbf{0} & \mathbf{0} & \mathbf{I}e^{i\mathbf{k}\cdot\mathbf{e_1}} & \mathbf{0}\\ \mathbf{0} & \mathbf{0} & \mathbf{I}e^{i\mathbf{k}\cdot\mathbf{e_2}} & \mathbf{0}\\ \mathbf{0} & \mathbf{0} & \mathbf{I}e^{i\mathbf{k}\cdot(\mathbf{e_1}+\mathbf{e_2})} & \mathbf{0}\\ \mathbf{0} & \mathbf{0} & \mathbf{0} & \mathbf{I}\end{bmatrix}}^{\mathbf{P}} \overbrace{\begin{bmatrix}\mathbf{\Psi_L}\\ \mathbf{\Psi_B}\\ \mathbf{\Psi_{BL}}\\ \mathbf{\Psi_I}\end{bmatrix}}^{\overline{\mathbf{\Psi}}} \tag{3.43}$$

The matrix system and its derivatives with respect to time can be summarized in the following variable changes:

$$\mathbf{\Psi} = \mathbf{P}\overline{\mathbf{\Psi}}; \quad \dot{\mathbf{\Psi}} = \mathbf{P}\dot{\overline{\mathbf{\Psi}}}; \quad \ddot{\mathbf{\Psi}} = \mathbf{P}\ddot{\overline{\mathbf{\Psi}}} \tag{3.44}$$

If the variable changes are carried out in equations 3.36 and 3.37, and the equation 3.36 is multiplied by the left by $\mathbf{P}^H$, the following equations are obtained:

$$\mathbf{P}^H\mathbf{M}\mathbf{P}\ddot{\overline{\mathbf{\Psi}}} + \mathbf{P}^H\mathbf{C}\mathbf{P}\dot{\overline{\mathbf{\Psi}}} + \mathbf{P}^H\mathbf{K}\mathbf{P}\overline{\mathbf{\Psi}} - \mathbf{P}^H\tilde{\mathbf{\Theta}}\mathbf{v_p} = \mathbf{P}^H\mathbf{f} \tag{3.45}$$

$$\tilde{\mathbf{C}}_\mathbf{p}\dot{\mathbf{v}}_\mathbf{p} + \tilde{\mathbf{R}}\mathbf{v_p} + \tilde{\mathbf{\Theta}}^t\mathbf{P}\dot{\overline{\mathbf{\Psi}}} = \mathbf{0} \tag{3.46}$$

To reduce the notation, the following variable changes are made: $\overline{\mathbf{M}} = \mathbf{P}^H\mathbf{M}\mathbf{P}$; $\overline{\mathbf{C}} = \mathbf{P}^H\mathbf{C}\mathbf{P}$; $\overline{\mathbf{K}} = \mathbf{P}^H\mathbf{K}\mathbf{P}$; $\overline{\mathbf{\Theta}} = \mathbf{P}^H\tilde{\mathbf{\Theta}}$; $\bar{\mathbf{f}} = \mathbf{P}^H\mathbf{f}$. With this we obtain the equations 3.47 and 3.48, which have the same form as the equations 3.36 and 3.37, but by having the Bloch conditions applied the matrices $\overline{\mathbf{M}}$, $\overline{\mathbf{C}}$ and $\overline{\mathbf{K}}$ will depend on the wave vector, as well as $\overline{\mathbf{\Theta}}$ and $\bar{\mathbf{f}}$ vectors.

$$\overline{\mathbf{M}}\,\ddot{\overline{\mathbf{\Psi}}} + \overline{\mathbf{C}}\,\dot{\overline{\mathbf{\Psi}}} + \overline{\mathbf{K}}\,\overline{\mathbf{\Psi}} - \overline{\mathbf{\Theta}}\mathbf{v_p} = \bar{\mathbf{f}} \tag{3.47}$$

$$\tilde{\mathbf{C}}_\mathbf{p}\dot{\mathbf{v}}_\mathbf{p} + \tilde{\mathbf{R}}\mathbf{v_p} + \overline{\mathbf{\Theta}}^t\,\dot{\overline{\mathbf{\Psi}}} = \mathbf{0} \tag{3.48}$$

Since the equations have the same form as those presented in previous sections, the state space is the same as in section 4.3 but with the change of variable made, in such a way that: $\dot{\mathbf{z}} = \overline{\mathbf{A}}\mathbf{z} + \overline{\mathbf{b}}$, where $\overline{\mathbf{A}}$ and $\overline{\mathbf{b}}$ are given by:

$$\overline{\mathbf{A}} = \begin{bmatrix} \mathbf{0} & \mathbf{I} & \mathbf{0} \\ -\overline{\mathbf{M}}^{-1}\overline{\mathbf{K}} & -\overline{\mathbf{M}}^{-1}\overline{\mathbf{C}} & \overline{\mathbf{M}}^{-1}\overline{\mathbf{\Theta}} \\ \mathbf{0} & -\tilde{\mathbf{C}}_\mathbf{p}^{-1}\overline{\mathbf{\Theta}}^t & -\tilde{\mathbf{C}}_\mathbf{p}^{-1}\tilde{\mathbf{R}} \end{bmatrix}; \quad \overline{\mathbf{b}} = \begin{bmatrix} \mathbf{0} \\ \bar{\mathbf{f}} \\ \mathbf{0} \end{bmatrix} \tag{3.49}$$

The dispersion diagrams can be obtained by solving the eigenvalue problem associated with matrix $\overline{\mathbf{A}}$.

3.5. Bandgap identification

The Floquet–Bloch periodic condition require evaluating the wave vector in the BZ, however, for time independent harmonic systems, the properties of a wave propagating along an axis do not depend on its sense, so the BZ can be halved as shown in figure 3.5a (when referring to the BZ in later sections it is referring to the upper half). On the other hand, it has been seen in the literature that to determine the size and location of the bandgaps in highly symmetric unit cells, the domain of the wave vectors can be limited to the contour of the irreducible Brillouin zone (IBZ), which corresponds to a reduction of the BZ due to all the symmetries of the lattice, and it is shown in figure 3.5b [55].

The bandgaps studied in this work are those that have their origin in the local resonances of the cantilevers incorporated in the unit cells, so they are located around their fundamental frequency. Figure 3.6 shows the dispersion diagram of a type I unit cell that is described in more detail in section 6.2. In figure 3.6a the wave vectors that run through the BZ are used, while in figure 3.6b the contour of the IBZ is used. In both figures the size and location of the bandgap is the same, so in this case no information about the bandgap is lost if the domain of the wave vectors is reduced to the contour of the IBZ, this is because type I unit cells are highly symmetric.

In both dispersion diagrams presented there is a horizontal band at a frequency of 1828.10 [Hz], which corresponds to the natural frequency of the resonators. The bandgap extends above and below this horizontal band, and they are called upper bandgap and lower bandgap

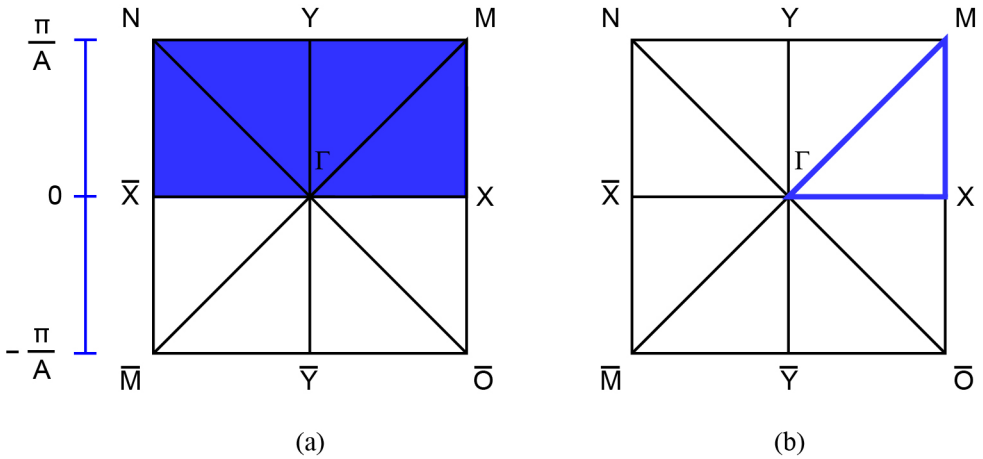

Figure 3.5: **(a)** Upper half of the Brillouin Zone (BZ) and **(b)** contour of the irreducible Brillouin zone (IBZ).

in this work, respectively. A constant dispersion band (independent of the wave vector) indicates that the wave is not propagated by the cell, which means that the lower and upper bandgap can be added to quantify the total bandgap generated by local resonances. The distinction is made between the upper and lower bandgap to quantify the contribution of each one to the total bandgap.

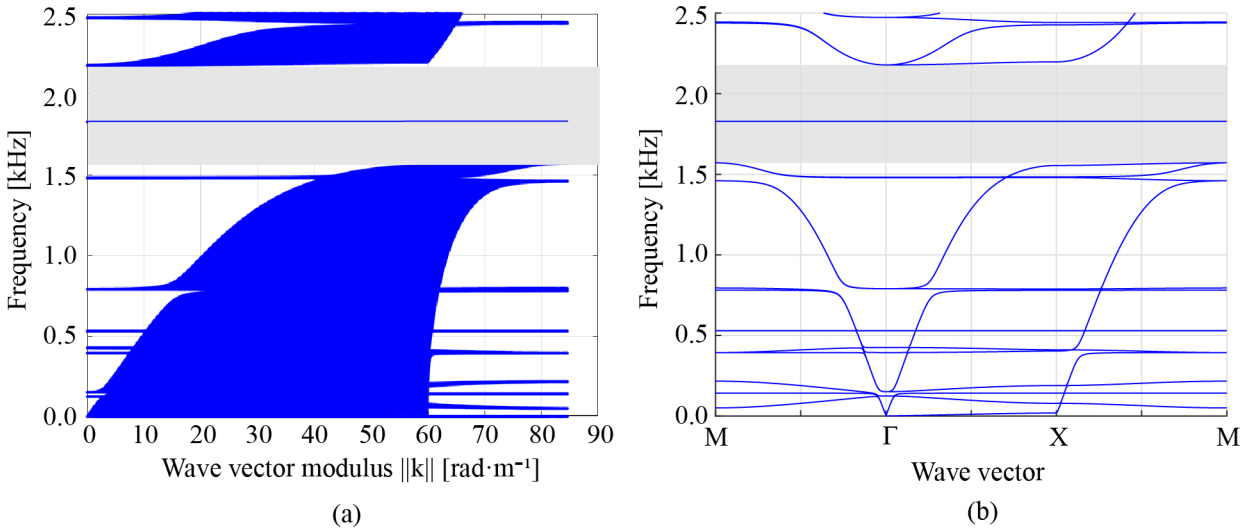

Figure 3.6: Dispersion diagrams of a type I unit cell, in which the domain of the wave vectors is considered **(a)** the entire the BZ and **(b)** in the contour of the IBZ.

To know the size and position of the bandgap, it is enough to evaluate the wave vector that gives the minimum frequency of the upper band of the bandgap and the wave vector that gives the maximum frequency of the lower band of the bandgap, which occurs at Γ for the upper band and at M for the lower band of figure 3.6b, these wave vectors are called "bandgap extrema" in this research, to be consistent with the nomenclature used by Maurin et al. [55] who did a study on bandgap extrema in porous phononic crystal. The problem

is that the bandgap extrema is not known in advance, and evaluating only some vectors can generate loss of valuable information, which can lead to overestimating the size of the bandgap or generate bandgaps that does not really exist, therefore, the full BZ should be evaluated to ensure that the results are correct.

3.6. Numerical Validation Approach

Figure 3.7 shows 3 square type I unit cells with their respective dispersion diagrams, which are performed by evaluating the wave vectors of the IBZ contour in the Floquet–Bloch periodic condition. Figure 3.7a corresponds to a square lattice, figure 3.7b to a square lattice with resonators and figure 3.7c to a square lattice with resonators and tip masses attached. The parameters used to evaluate the model are presented in table 3.1, where the difference is made between the beams that make up the square matrix and the elements that are used as resonators in cases b and c, the material used in all elements is acrylonitrile butadiene styrene (ABS).

The fundamental bending natural frequency of a resonator beam is given by $f_1 = \frac{1.875^2}{2\pi}\sqrt{\frac{EI}{\rho AL^4}}$ [56], where E, I, ρ, A and L are the Young's modulus, moment of inertia, density, area and length for the resonator beam, respectively. Evaluating the material and geometric parameters of the table 3.1, we can get $f_1 = 684.6[Hz]$, which coincides with the horizontal line that falls in the bandgap seen in figure 3.7b. On the other hand, if a tip mass is added to the resonators, an approximation of the fundamental frequency is given by $f_1^{Tip\ Mass} = \frac{1}{2\pi}\sqrt{\frac{3EI/L^3}{(33/140)\rho AL+M_t}}$ [57], where M_t corresponds to the tip mass. If the resonator parameters are evaluated, it follows that $f_1^{Tip\ Mass} = 145.1[Hz]$, which coincides with the horizontal line that falls in the bandgap of figure 3.7c.

The results obtained are consistent with what is found in the literature [1], and allow us to appreciate how the incorporation of resonators can generate bandgaps at low frequencies, specifically around the fundamental frequencies of the resonators.

Table 3.1: Geometric and material parameters of the substructure of the matrix beams and the resonators (Res.) [1].

Geometric parameters	Matrix Beams	Res.	Material parameters	Matrix Beams	Res.
Length, L (mm)	35	13.98	Mass density, ρ $(kg\,m^{-3})$	1099	1099
Width, b (mm)	10	10	Young's mod., Y (MPa)	1900	1900
Thickness, h (mm)	1	0.63	Tip mass, M_t (gm)	-	0.5

To find the appropriate mesh refinement for the finite element model, a type I unit cell is divided into 8, 16, 24, 32, 40 and 80 elements. Both the matrix beams and the resonators are divided into the same number of elements, so if the cell is divided into 40 elements it means that each beam and resonator is divided into 5 elements (type I is made up of 4 matrix beams and 4 resonators). The physical and geometric properties of the substructure are those

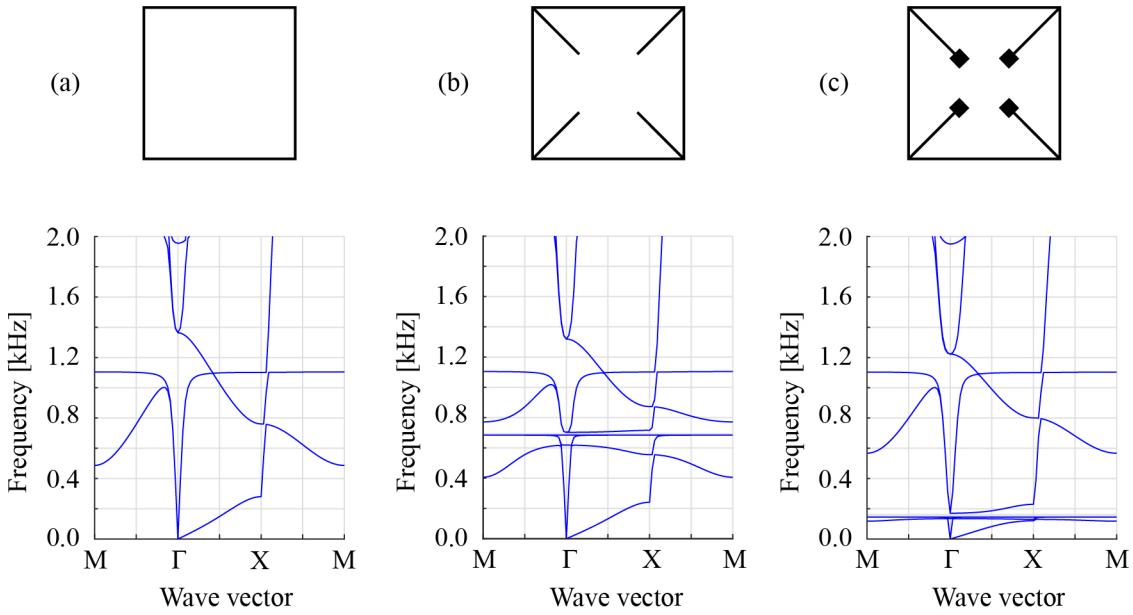

Figure 3.7: Topologies of the type I unit cell and the corresponding dispersion diagrams: **(a)** original square lattice, **(b)** modified square lattice with resonators, and **(c)** modified square lattice with resonators and tip masses attached.

indicated in table 3.1, and the piezoelectrics considered in the bimorph resonators are PVDF whose properties are indicated in table 3.2. The dispersion diagrams of each refinement are presented in figure 3.8.

Table 3.2: Geometric, material and electromechanical properties of PVDF layers of the bimorph harvesters [58].

Geometric parameters	Piezo. PVDF	Material parameters	Piezo. PVDF
Length, L (mm)	13.98	Mass density, ρ $(kg\,m^{-3})$	1780
Width, b (mm)	10	Young's modulus, Y (GPa)	3
Thickness, h (mm)	0.028 (each)	Piezo. Constant, d_{31} (pmV^{-1})	-23
		Permittivity, $\bar{\varepsilon}^{s}_{33}$ (pFm^{-1})	106

To quantify the results, the fundamental natural frequency of the resonators and the bandgap size are measured. These results are presented in table 3.3. From the results presented, it can be observed that with 24 elements (3 for each beam and resonator) sufficiently precise results are obtained, so considering that number of divisions is reasonable for the model. If unit cells with more resonators are used, more elements must be considered, in the case of a type IV unit cell, 36 elements would have to be considered to maintain the same 3 for each beam and resonator.

To validate the electromechanically coupled finite element model, the results obtained are compared with the analytical multi-mode model presented by Erturk and Inman [51], for a resonator bimorph harvester configuration with a tip mass under base excitation, whose

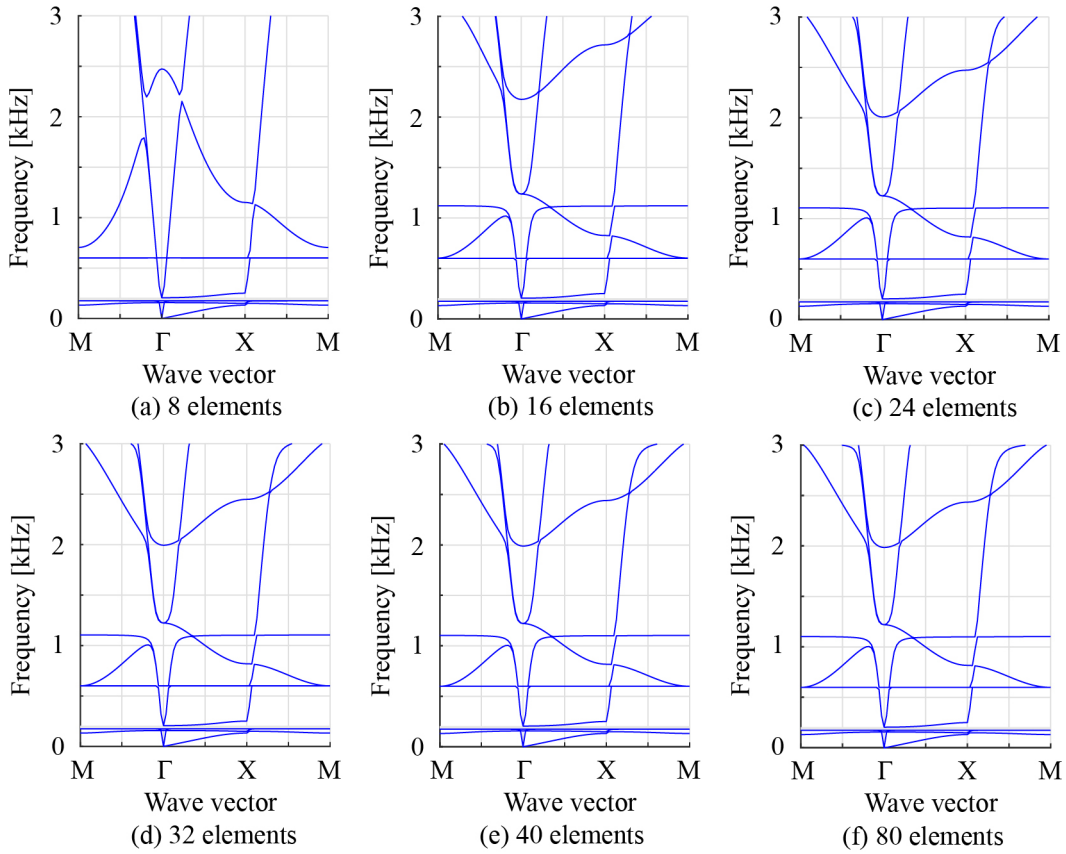

Figure 3.8: Dispersion diagrams with different mesh refinements for a type I unit cell containing bimorph harvester resonators, and whose properties are indicated in tables 3.1 and 3.2. The diagrams consider mesh refinements with **(a)** 8, **(b)** 16, **(c)** 24, **(d)** 32, **(e)** 40 and **(f)** 80 elements.

piezoelectric layers has a series connection (as presented in figure 3.9 b). The geometry and materials used for the substructure and the piezoelectric layers are presented in table 3.4.

Equations 3.38 and 3.39 allow obtaining the electromechanical FRFs. The mass, stiffness, damping, coupling term, effective capacitance and vector forcing matrices must be modified accordingly to account for the effect the effect of the additional piezoelectric layer. In addition, the tip mass must be included in the extreme elements of the resonators.

Figure 3.10 presents the results of the FRFs obtained for 8 resistance values (1 kΩ, 7 kΩ, 22 kΩ, 47 kΩ, 100 kΩ and 470 kΩ), considering 10 modes in the Erturk and Inman model and a discretization of 10 elements in the FE model. In the case of the FE model, the displacement and speed correspond to the vertical degree of freedom of the free end of the resonator. The mechanical FRFs obtained from the FE model are in agreement with the analytical multi-mode model results.

Table 3.3: Resonator frequency and bandgap size for the 6 mesh refinements considered in figure 3.8.

Number of FE	Resonator frequency [Hz]	Bandgap [Hz]
8	174.802	31.233
16	174.800	31.053
24	174.800	31.043
32	174.800	31.042
40	174.800	31.041
80	174.800	31.041

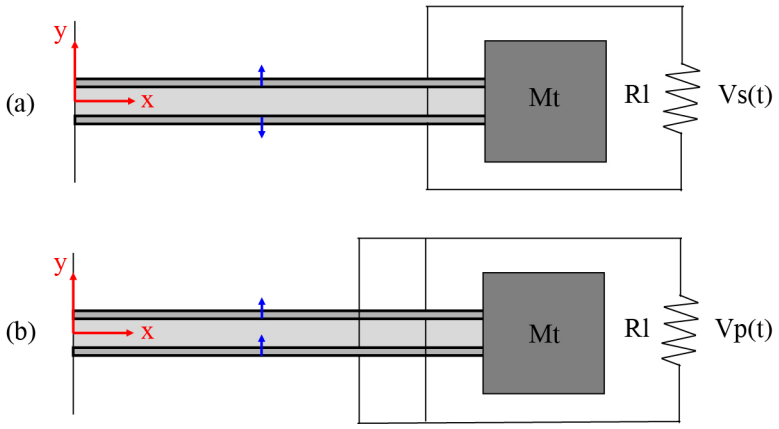

Figure 3.9: Bimorph cantilever configurations with **(a)** series and **(b)** parallel connection of piezoelectric layers.

Table 3.4: Geometric, material and electromechanical properties of the substructure (brass) and piezoelectric layers (PZT-5A) for a bimorph harvester [51].

Geometric parameters	Piezo.	Sub.	Material parameters	Piezo.	Sub.
Length, L (mm)	50.8	50.8	Mass density, ρ $(kg\,m^{-3})$	7800	9000
Width, b (mm)	31.8	31.8	Young's mod., Y (Gpa)	66	105
Thickness, h (mm)	0.26 (each)	0.14	Piezo. Cons., $d_{31}(pmV^{-1})$	-190	-
Tip mass, $M_t(kg)$	0.012		Permittivity, $\bar{\varepsilon}^s_{33}$ $(F\,m^{-1})$	$1500\epsilon_0$	-

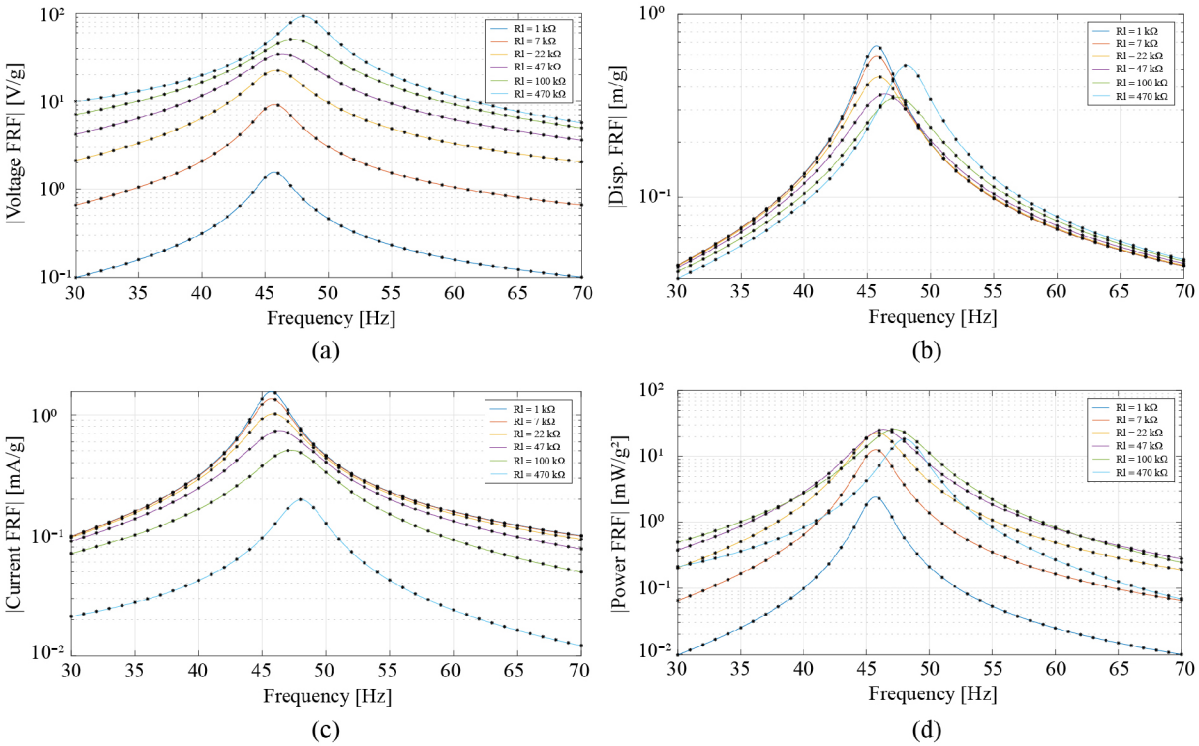

Figure 3.10: **(a)** Voltage FRF, **(b)** tip displacement FRF, **(c)** current FRF and **(d)** power FRF for 6 different values of load resistance (the electromechanically coupled finite element model are the colored lines, while the analytical multi-mode model presented by Erturk and Inman are presented as black asterisks).

Chapter 4

Bandgap and its relation with the wave vector

In this section we study whether it is possible to reduce the domain of wave vectors to identify bandgaps due to local resonances for the 6 types of unit cells of figure 2.2. The methodology used consists in choosing an initial unit cell configuration of any of the 6 types analyzed, and perform 10,000 different random variations of all the original parameters. These variations have a value less than or equal to 50% of the original parameters, this range of variation is defined arbitrarily in order to achieve configurations that make physical sense (if it is not limited, there could be cases with very large resonators compared to the matrix beams, very large tip masses for the rigidity of the resonators or other incompatibilities) and that are in a limited area around the original configuration (there are clearly physically possible configurations that are beyond the range of variation, which may eventually result in unit cells much larger or much smaller than the original cell). Each time the properties are varied randomly, the dispersion diagrams are calculated covering the BZ (blue area of the figure 3.5a), and the bandgap extrema are identified. In this way, it is possible to see if for this type of resonators it is reasonable to reduce the domain of wave vectors to the contour of the IBZ as was done in figure 3.6b, or if the domain could be reduced even further.

To correctly interpret the results of subsequent sections, it should be noted that in each of the 10,000 random variations of the parameters, the length of the beams of the matrix is varied, which generates changes in the dimensions of the BZ. This is why a BZ with a unit side (normalized BZ) is defined, which is used to compare the locations of the wave vectors in cells that have different dimensions. Normalization simply consists of dividing the components of the identified wave vector by $\frac{\pi}{A}$, where A is the periodicity of the unit cell (length of the matrix beams) obtained from the random variation of parameters.

4.1. Bandgap Location - Case 1: Types I and IV unit cells

Type I and IV unit cells have several axes of symmetry, therefore, when making the random variation of parameters, the required symmetries must be maintained, which implies that an angle of 45° must be maintained for type I cells, and that there is only one degree of freedom to vary the angles of type IV unit cells (if all angles change independently, symmetry is lost).

The initial configuration of the type I and type IV unit cells on which the random variations are performed considers the properties of the tables 3.1 and 3.2 (the 2 cantilevers of each node of type IV unit cells must have the same properties to maintain symmetry).

The results obtained when applying the random variations for the type I and type IV unit cells indicate that to obtain the size and position of the bandgap, it is enough to evaluate the wave vectors that are located at N, Y, M, $\bar{X}$ and Γ, i.e., in none of the random variations the upper and lower bandgap extrema was found in another wave vector different from those mentioned. The percentage of times that the upper and lower bandgap extrema is found in each of these wave vectors is indicated in table 4.1. In both type I and type IV unit cells, the upper bandgap extrema is found predominantly in the Γ wave vector, while the lower bandgap extrema is found mainly between the M and N wave vectors.

Figures 4.1 and 4.2 show scatter plots of the bandgap versus the resonator frequency for the upper and lower bandgap for type I and type IV unit cells, respectively. The bandgaps are presented as percentages with respect to the frequency of the resonators, and the graphs were grouped according to the bandgap extrema, which is indicated at the top of each graph. The results show that as the resonators stiffen, higher values are obtained for the lower bandgap, while the upper bandgap does not show frequency dependence.

Table 4.1: Percentage of times that the upper and lower bandgap extrema is located in each wave vector, with respect to the 10,000 random variations of type I and type IV unit cells.

Wave Vector	Type I		Type IV	
	Upper Bandgap [%]	Lower Bandgap [%]	Upper Bandgap [%]	Lower Bandgap [%]
N	1.19	48.95	1.91	48.25
$\bar{X}$	1.12	1.35	0.98	1.24
Γ	95.18	0.02	94.38	0.03
Y	1.14	1.06	1.09	1.13
M	1.37	48.62	1.54	49.35

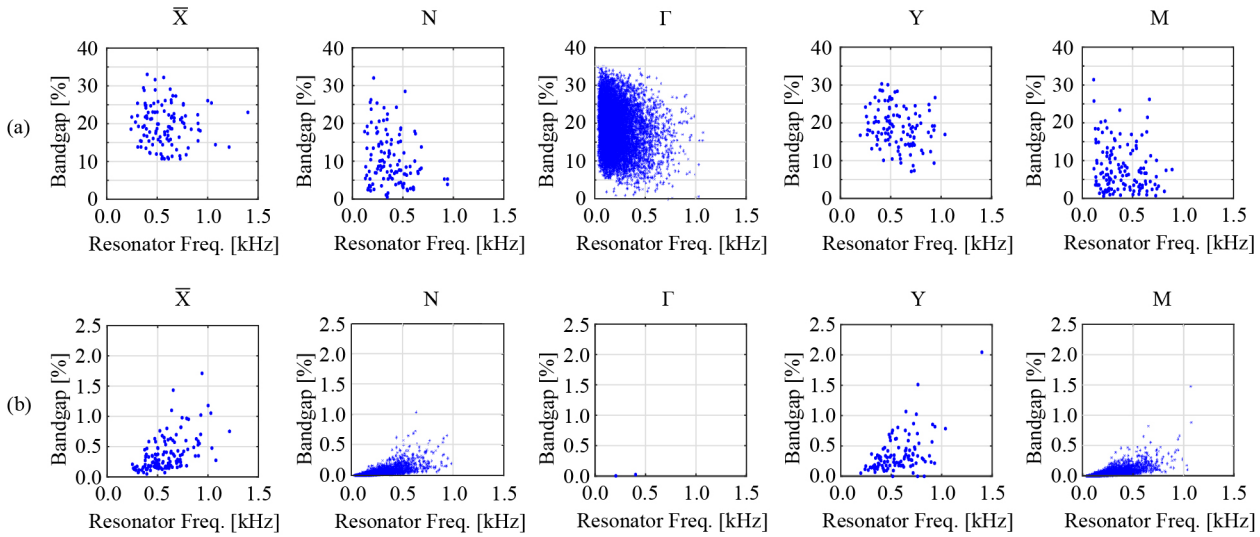

Figure 4.1: Bandgap size (as a percentage of resonator frequency) versus resonator frequency for **(a)** upper and **(b)** lower bandgap in type I unit cells. In each case, the bandgap extrema is indicated.

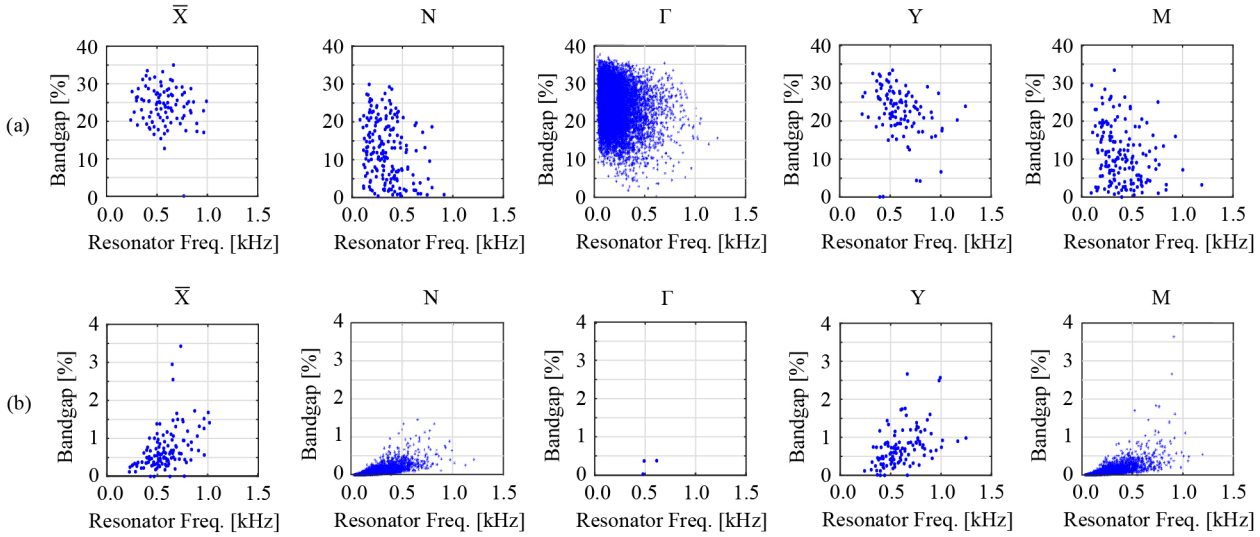

Figure 4.2: Bandgap size (as a percentage of resonator frequency) versus resonator frequency for **(a)** upper and **(b)** lower bandgap in type IV unit cells. In each case, the bandgap extrema is indicated.

4.2. Bandgap Location - Case 2: Types II and V unit cells

Type II and V unit cells have no symmetry requirements, so all resonator angles are varied independently in each of the random variations. The initial configuration of the type II unit cell on which the random variations are performed considers the properties of the tables 3.1 and 3.2. For type V unit cell, the same properties are considered, but in this case there is an additional resonator at each node, which starts with the properties of tables 3.1 and 3.2, but considering half of the tip mass and half length ($0.5M_t$ and 0.5L), these modifications cause

this additional resonator to have a higher frequency, so it is called high frequency resonator and the other is called low frequency resonator (with random variations it could happen that the resonator that initially has a lower frequency remains with a higher frequency, but the names are used only to differentiate them).

The results obtained when applying the random variations for the type II and type V unit cells indicate that to obtain the size and position of the bandgap, it is enough to evaluate the wave vectors that are located at N, Y, M, $\bar{X}$ and Γ, i.e., in none of the random variations the upper and lower bandgap extrema was found in another wave vector different from those mentioned. The percentage of times that the upper and lower bandgap extrema is found in each of these wave vectors is indicated in table 4.2. In the case of type II unit cells, a behavior similar to that of type I and type IV is obtained, with Γ being the predominant wave vector for the upper bandgap extrema and for the lower bandgap extrema it is distributed mainly between M and N. On the other hand, in type V unit cells, it happens that the bandgaps associated with the low frequency resonators behave the same as those of type I, II and IV unit cells, but the bandgaps associated with the high frequency resonators have higher percentages associated with the vectors $\bar{X}$ and Y for both the upper bandgap and the lower bandgap.

Figure 4.3 shows the scatter plot of the bandgap versus the resonator frequency for the upper and lower bandgap for type II unit cell. Since type V unit cells allow having 2 resonators with different natural frequencies, the scatter plots for each type of resonator are differentiated, and are presented in figures 4.4 and 4.5 for each resonator. The results obtained agree with those seen for type I and type IV unit cells, and figure 4.5b shows that the size of the upper bandgap increases considerably for high frequencies of the resonators.

Table 4.2: Percentage of times that the upper and lower bandgap extrema is located in each wave vector, with respect to the 10,000 random variations of type II and type V unit cells. This last type of cell allows the incorporation of 2 cantilevers with different frequencies, which generate 2 bandgaps, which are indicated separately.

Wave Vector	Type II		Type V			
			Low freq. Resonator		High freq. Resonator	
	Upper Bandgap [%]	Lower Bandgap [%]	Upper Bandgap [%]	Lower Bandgap [%]	Upper Bandgap [%]	Lower Bandgap [%]
N	0.56	49.22	0.65	49.88	2.05	42.49
$\bar{X}$	1.15	0.44	0.95	0.45	11.69	6.94
Γ	96.77	0.05	96.94	0.05	71.99	0.48
Y	0.93	0.52	0.93	0.43	12.17	6.53
M	0.59	49.77	0.53	49.19	2.1	43.56

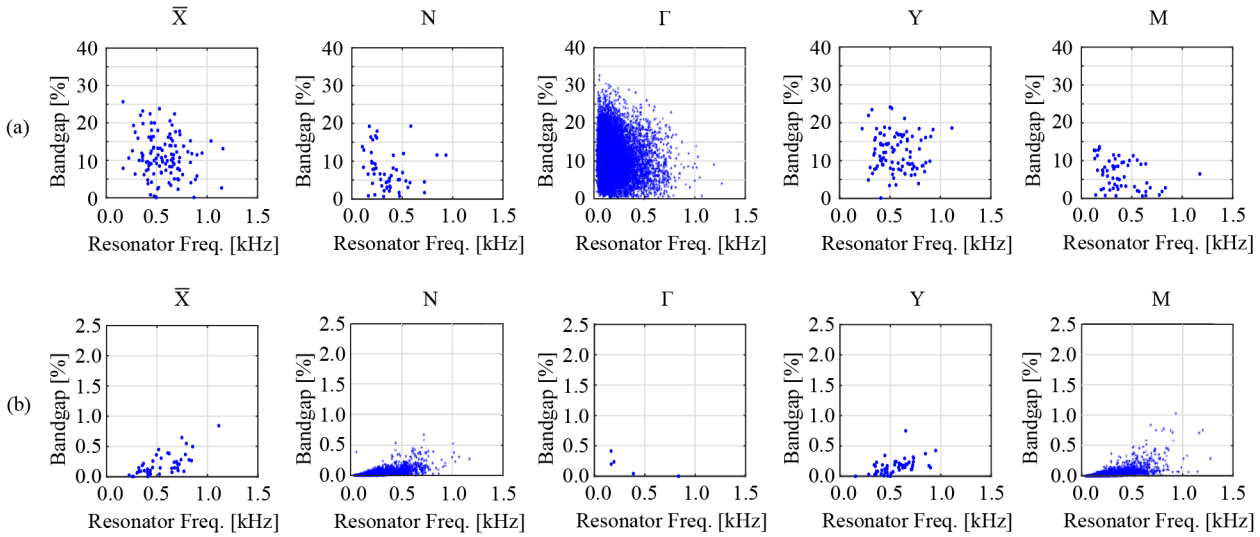

Figure 4.3: Bandgap size (as a percentage of resonator frequency) versus resonator frequency for **(a)** upper and **(b)** lower bandgap in type II unit cells. In each case, the bandgap extrema is indicated.

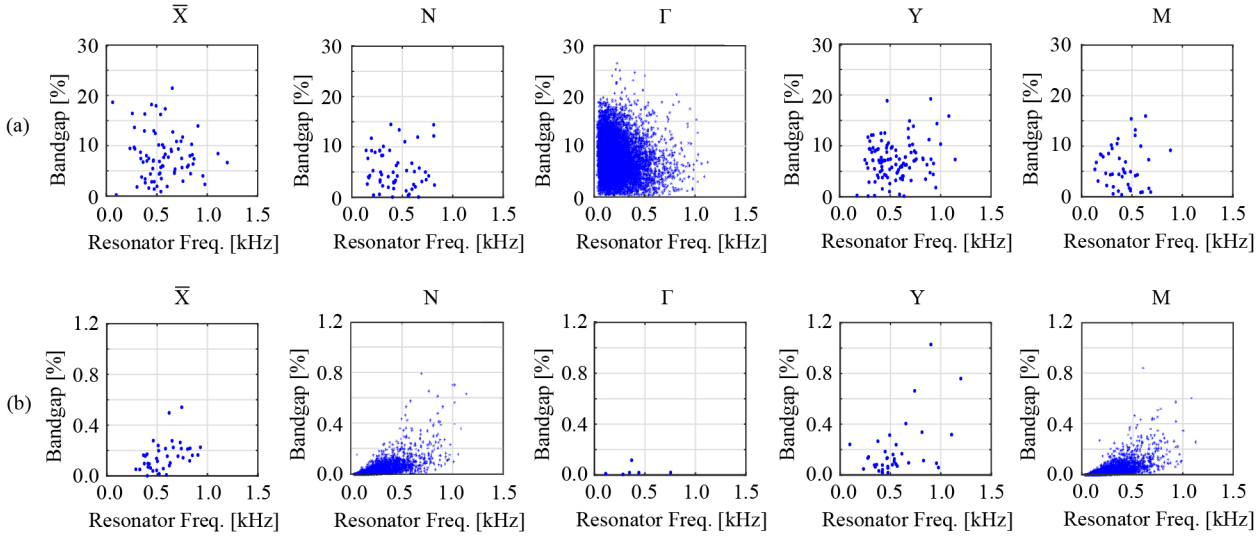

Figure 4.4: Bandgap size (as a percentage of resonator frequency) versus resonator frequency for **(a)** upper and **(b)** lower bandgap in type V unit cells low frequency resonators. In each case, the bandgap extrema is indicated.

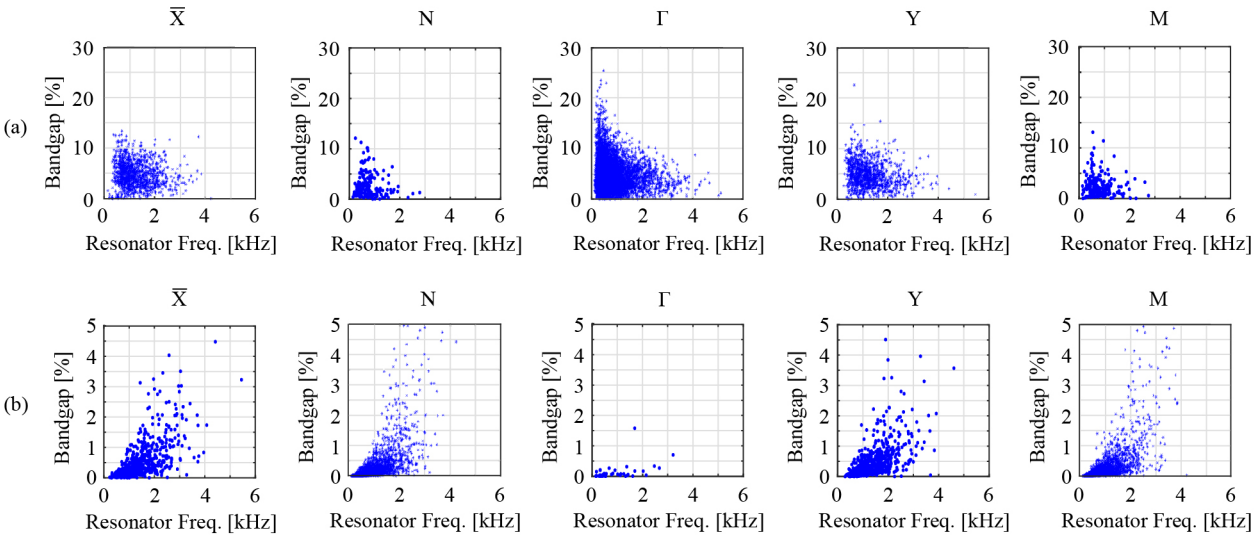

Figure 4.5: Bandgap size (as a percentage of resonator frequency) versus resonator frequency for **(a)** upper and **(b)** lower bandgap in type V unit cells high frequency resonators. In each case, the bandgap extrema is indicated.

4.3. Bandgap Location - Case 3: Types III and VI unit cells

Type III and VI unit cells do not always generate bandgaps due to local resonances, therefore, it is not possible to carry out the analysis presented for the other types of unit cells. This is why an example of the dispersion diagrams for each type of cell is presented, in which the wave vectors in the entire BZ are evaluated.

For the type III example, the properties of tables 3.1 and 3.2 are considered for the substructure and the piezoelectric, respectively. To achieve the required asymmetry in this type of cell the tip mass of each cantilever is modified, the values considered in terms of M_t (mass indicated in table 3.1) are $0.5M_t$, M_t, $1.5M_t$ and $2M_t$, which correspond to resonators with natural frequencies of 241.30 [Hz], 174.80 [Hz], 143.91 [Hz] and 125.16 [Hz], respectively. In the case of type VI example, 4 cantilevers are added to those already mentioned, whose tip masses are $0.25M_t$, $3M_t$, $3.5M_t$ and $4M_t$, which correspond to resonators with natural frequencies of 326.12 [Hz], 102.63 [Hz], 95.13 [Hz] and 89.07 [Hz], respectively.

Figures 4.6a and 4.6b show the dispersion diagrams for the type III and type VI unit cell, respectively. It can be seen that no bandgaps are generated in the resonator frequencies in either type of unit cell.

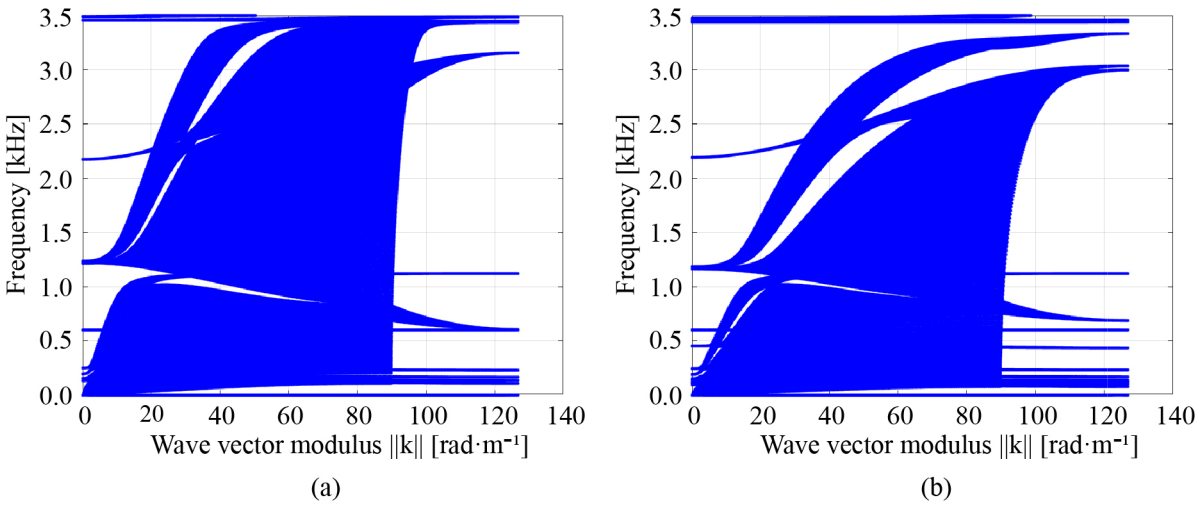

Figure 4.6: Examples of dispersion diagrams for **(a)** type III and **(b)** type VI unit cells.

Chapter 5

Parametric Study

In this section, a parametric analysis is performed for type I and type V unit cells. This analysis consists in defining nominal properties to the unit cell, and varying the value of each physical and geometric parameter of the model by 50% (up and down), this percentage of variation is defined in such way that the structure remains geometrically and physically possible (if the properties are varied a lot, it can happen that the cantilevers are excessively large compared to the matrix or that the tip mass is too large for the rigidity of the cantilevers). What is measured is the variation that occurs in the size and location of the bandgap associated with the local resonances of the cantilevers.

The bandgaps are presented as a percentage with respect to the resonator frequency (after varying the corresponding parameter), this way of measuring bandgaps is very convenient to keep the bandgap at low frequencies since parameters that increase the bandgap but at the same time increase the frequency of the cantilever are penalized.

5.1. Case 1: Single Resonator

The original configuration corresponds to a type I unit cell, whose substructure and piezoelectric layers properties are indicated in table 3.1 and 3.2, respectively. The results of the parametric analysis are presented in figure 5.1 as graphs of resonator frequency in Hz versus total bandgap presented as the percentage with respect to the resonator frequency. The graphs are grouped into 4 categories: geometric properties of the matrix, geometric properties of resonators, physical properties of piezoelectric layers and physical properties of substructure.

The extreme values of the parametric analysis are summarized in tables 5.1 and 5.2, which correspond to a variation of -50% and +50% with respect to the original values, respectively. These tables are very useful because the variation of parameters in the ranges used generate strictly increasing, strictly decreasing or constant variations, this is why the extreme values give information about the maximum or minimum values. The only parameter that escapes this rule is the resonator length, which presents a maximum when there is an increase close to 50%, so the value in the table is a little lower than the maximum value of the parametric analysis for this parameter (this variation is irrelevant for the ranges of variation studied, but could be an important phenomenon in other cases).

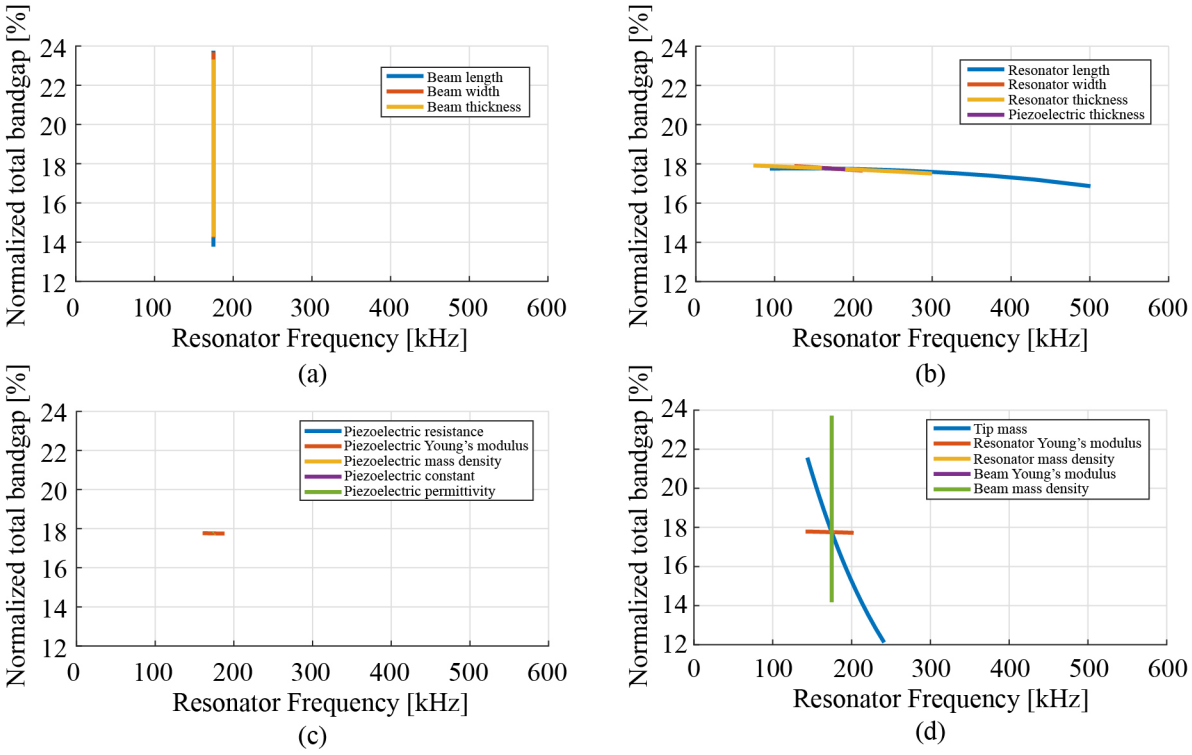

Figure 5.1: Parametric analysis for type I unit cells, in which the properties are varied in a range of ±50% with respect to the original ones. The parameters are grouped into 4 categories: **(a)** geometric properties of the matrix, **(b)** geometric properties of resonators, **(c)** physical properties of piezoelectric layers and **(d)** physical properties of substructure.

The second column of the tables presents a dimensionless value that corresponds to the ratio between the frequency of the cantilever varying the indicated parameter and the original frequency of the cantilever using the nominal values. In the third and fourth column, additional information is provided to the figure 5.1, since it differentiates between the upper and the lower bandgap. The fifth column presents the same information as the figure. The rows of the tables are ordered in such way that they are divided into 3 groups, the first corresponds to the rows that have a frequency ratio value less than 1, the second to those that have a value equal to 1, and the third to those with a value greater than 1. Within these groups they are ordered according to the total bandgap from lowest to highest.

If the results obtained in the tables are compared, it can be seen in which direction the model parameters should move in order to obtain a larger bandgap:

- To enlarge the upper and total bandgap, the following modifications must be made:
  - Increase the following parameters: beam Young's modulus, piezoelectric resistance, piezoelectric $\bar{\varepsilon}^s_{33}$, tip mass, resonator length and piezoelectric e_{31}.
  - Decrease the following parameters: piezoelectric Young's modulus, resonator Young's modulus, beam thickness, beam width, beam mass density, beam length, piezoelectric thickness, resonator width, resonator thickness, piezoelectric mass density and

Table 5.1: Values of the parametric analysis for type I unit cell when decreasing the original properties by 50%.

Parameter	Frequency ratio	Upper band gap [%]	Lower band gap [%]	Total band gap [%]
Piezoelectric Young's modulus	0.92	17.76	0.01	17.77
Resonator Young's modulus	0.81	17.78	0.01	17.79
Piezoelectric thickness	0.92	17.77	0.01	17.79
Resonator width	0.72	17.88	0.01	17.89
Resonator thickness	0.42	17.91	0.00	17.92
Beam Young's modulus	1.00	17.63	0.03	17.66
Piezoelectric e_{31}	1.00	17.74	0.02	17.75
Piezoelectric resistance	1.00	17.74	0.02	17.75
Piezoelectric $\overline{\varepsilon}^s_{33}$	1.00	17.74	0.02	17.76
Piezoelectric mass density	1.00	17.75	0.02	17.77
Beam thickness	1.00	23.27	0.03	23.30
Beam width	1.00	23.65	0.03	23.68
Beam mass density	1.00	23.70	0.02	23.72
Beam length	1.00	23.75	0.01	23.75
Tip mass	1.38	12.10	0.02	12.12
Resonator length	2.86	16.74	0.12	16.87
Resonator mass density	1.01	17.81	0.02	17.83

resonator mass density.

- To enlarge the lower bandgap, the following modifications must be made:
  - Increase the following parameters: resonator mass density, beam length, beam mass density, piezoelectric $\overline{\varepsilon}^s_{33}$, piezoelectric resistance, piezoelectric mass density, resonator Young's modulus, resonator thickness, piezoelectric Young's modulus, piezoelectric thickness, resonator width and piezoelectric e_{31}.
  - Decrease the following parameters: beam Young's modulus, beam thickness, beam width, tip mass and resonator length.

From the results obtained, it can be seen that the greatest benefits are obtained by reducing 50% some parameters associated with the matrix beams: density, length, width and thickness. Varying these parameters generates a double benefit, since not only generate the greatest increases in the bandgap, but they also keep the resonator frequency constant (frequency ratio equal to 1). This allows you to control the bandgap location by designing the cantilevers and then optimize the bandgap size by modifying the parameters of the matrix beams without changing the bandgap location. The beam Young's modulus can be added to the mentioned parameters, although it does not generate a great increase in the bandgap, it still allows the cantilever frequency to be keep constant.

Table 5.2: Values of the parametric analysis for type I unit cell when increasing the original properties by 50%.

Parameter	Frequency ratio	Top band gap [%]	Lower band gap [%]	Total band gap [%]
Resonator mass density	0.99	17.69	0.02	17.70
Resonator length	0.54	17.75	0.00	17.76
Tip mass	0.82	21.55	0.02	21.57
Beam length	1.00	13.75	0.02	13.78
Beam mass density	1.00	14.16	0.02	14.17
Beam width	1.00	14.21	0.01	14.22
Beam thickness	1.00	14.27	0.01	14.28
Piezoelectric mass density	1.00	17.73	0.02	17.75
Piezoelectric $\overline{\varepsilon}^s_{33}$	1.00	17.74	0.02	17.76
Piezoelectric resistance	1.00	17.75	0.02	17.76
Piezoelectric e_{31}	1.00	17.75	0.02	17.77
Beam Young's modulus	1.00	17.78	0.01	17.79
Resonator thickness	1.71	17.46	0.05	17.51
Resonator width	1.21	17.63	0.02	17.66
Resonator Young's modulus	1.16	17.70	0.02	17.72
Piezoelectric thickness	1.08	17.71	0.02	17.73
Piezoelectric Young's modulus	1.08	17.73	0.02	17.75

The physical properties of the piezoelectric also have a frequency ratio equal to 1 (mass density, resistance, $\overline{\varepsilon}^s_{33}$ and e_{31}), but care must be taken with these properties because the frequencies of the cantilevers change in a very small amount which is not appreciable due to the limited range of variation that is considered ($\pm 50\%$), but larger variations could generate appreciable frequency changes. These properties generate very small variations in the bandgap size.

Vary the physical and geometric properties of the cantilevers produce large changes in their frequency (especially varying the geometric ones), but not all of them generate large variations in the bandgap. Among these properties, the one that generates the greatest benefit is the tip mass, since it allows the relative bandgap to be increased as the resonator frequency is reduced.

5.2. Case 2: Double Resonator

The original configuration corresponds to a type V unit cell, whose substructure and piezoelectric layers properties are indicated in table 3.1 and 3.2, respectively (the 8 resonators have the same properties initially). The parametric analysis carried out is different from the one presented in section 6.1, since this time we want to change the properties of one of the two resonators of each node, keeping the properties of the other resonator constant, to

see the relationship that exists between the bandgaps generated by both resonators (each node will have a resonator with the initial properties, and another resonator that changes its properties according to the analysis performed).

The results of the parametric analysis are presented in figure 5.2 as graphs of the percentage difference between the frequency of the resonator that is varied and the one that remains constant versus frequency presented as a percentage with respect to the frequency of the resonator that maintains the original properties. Only the graphs associated with the parameters whose variation appreciably modifies the frequency of the resonator were included. In each graph there is a black zone that corresponds to the total bandgap generated by the resonators that maintain their original properties, and a red zone that corresponds to the bandgap generated by the resonators that change in frequency.

From the results it is obtained that the bandgap associated with the lower frequency resonator is reduced due to the higher frequency resonator, which is clearly seen in the black zone, which decreases sharply after crossing the red zone, and then it increases as the red zone moves to higher frequencies and has less influence on the black zone. The red zone exhibits a similar behavior, as it has a very small width when it is below the black zone, and increases once it is above it. It should be taken into account that once the red zone is at the top, its width can decrease or increase depending on the frequency of the resonator, and this variation is consistent with what is obtained in the parametric analysis of section 6.1.

The largest size of the bandgap associated with the resonator that maintains the original properties (black zone) is 23.68% and occurs when both zones intersect, which means that it occurs when all the resonators have the original properties. The bandgap size of the type I unit cell used in section 5.1 has a value of 17.76% (point of intersection of the curves in figure 5.1), which means that adding several resonators with the same properties in the same node allows to increase the size of the bandgap.

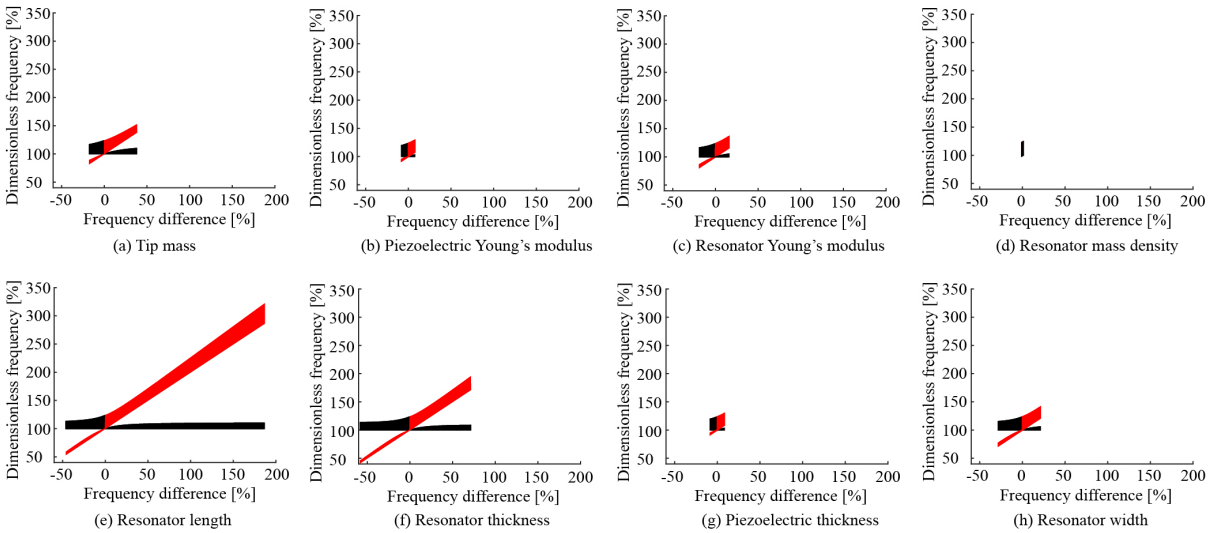

Figure 5.2: Parametric analysis for type V unit cells, in which the properties of one of the resonators of each node remain unchanged, and those of the other are varied in a range of $\pm 50\%$ with respect to the original ones. The horizontal axis indicates the frequency difference in percentage between the resonator that varies its properties and the one that keeps them constant, on the other hand, the vertical axis corresponds to the frequency measured as a percentage with respect to the frequency of the original resonator. The red zone indicates the total bandgap of the resonator whose parameters are varied, while the black zone indicates the bandgap of the resonator that maintains its original properties.

Chapter 6

Effects of the simultaneous variation of parameters on the bandgap

In this section, the behavior of the bandgap is analyzed when combining the variations of various parameters of the model, for which 2 interesting cases that emerge from the parametric analysis of section 5.1 are analyzed. The first case corresponds to varying the parameters of the matrix to widen the upper and lower bandgap without modifying the original frequency of the resonator. In the second case, the same objective is sought, but all the parameters are varied regardless of whether the frequency of the resonators changes. In both cases, the parameters are varied by the same percentage starting from 0% up to a 50% variation (it can be an increase or a decrease depending on what the parametric analysis indicates). In addition, the most favorable dispersion curves for each case are presented.

6.1. Case 1: Optimize bandgap while maintaining resonator frequency

According to the results of the parametric analysis of section 5.1, by modifying the parameters of the matrix beams, the size of the bandgap can be modified while maintaining the frequency of the resonators.

To enlarge the upper and total bandgap, the density, length, width and thickness of the matrix beams should decrease, and the beam Young's modulus of the matrix beam should increase. Figures 6.1a, 6.1b and 6.1c show the bandgap as a percentage of the resonator frequency depending on the percentage of variation of the parameters of the matrix beams (all vary by the same percentage in the indicated directions) for the upper, lower and total bandgap, respectively. Figure 6.1d shows the number of bands that remain below the resonator band, and figure 6.1e shows the frequency of the resonator as the parameters are varied.

The results obtained agree with what was expected, since the frequency of the resonator does not vary and the upper and total bandgap have a significant increase as the parameters are varied. This increase is greater than that obtained by varying the parameters individually in section 5.1, and it reaches its maximum value when all the parameters are varied by 50% with respect to the original ones.

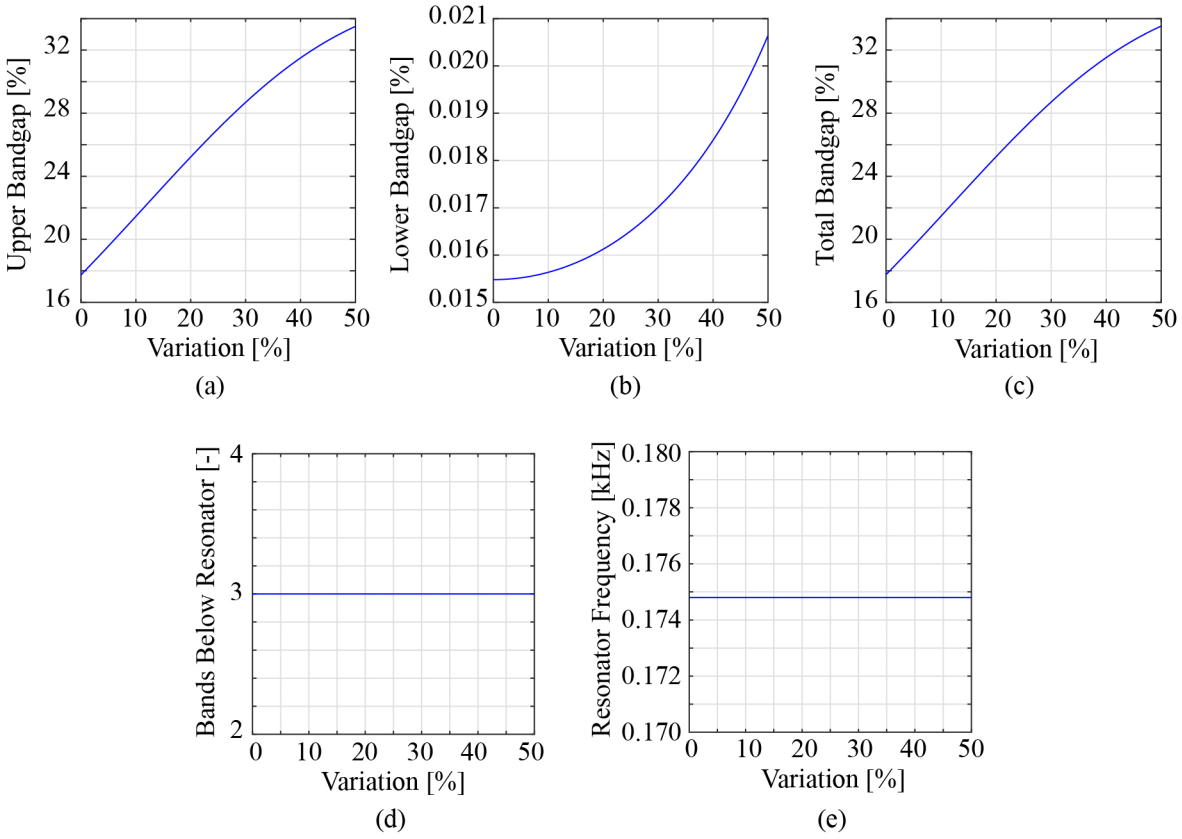

Figure 6.1: **(a)** Upper, **(b)** lower and **(c)** total bandgap for variations between 0% and 50% of the parameters of the matrix beams in the direction in which they increase the upper and total bandgap. No changes are generated in the **(d)** number of bands below the resonator nor in **(e)** the frequency of the resonators.

On the other hand, to enlarge the lower bandgap, the Young's modulus, width and thickness of the matrix beams should decrease, and the density and length of the matrix beams should increase. Figure 6.2 shows the results for this case, which also behave as expected, since the frequency of the resonators remains constant and the lower bandgap increases considerably. However, there is an abrupt change in the curves, since when the parameters are varied by 45.3% the bandgap goes to 0, and then grows rapidly, which is accompanied by an increase from 3 to 5 in the bands below the resonators. This phenomenon occurs because in order to enlarge the lower bandgap, the matrix beams must be made more flexible, which causes their associated bands to drop to lower frequencies, which may even be lower than the frequency of the resonators.

This fact is relevant when performing an optimization, since the objective function that describes the bandgap has abrupt changes when the number of bands under the resonator changes, so one way to attack the problem can be to optimize given a number of bands below the frequency of the resonator.

To see the phenomenon mentioned above, a sequence of 6 configurations is made, whose dispersion curves are presented in figure 6.3, in which figure a) uses the original properties

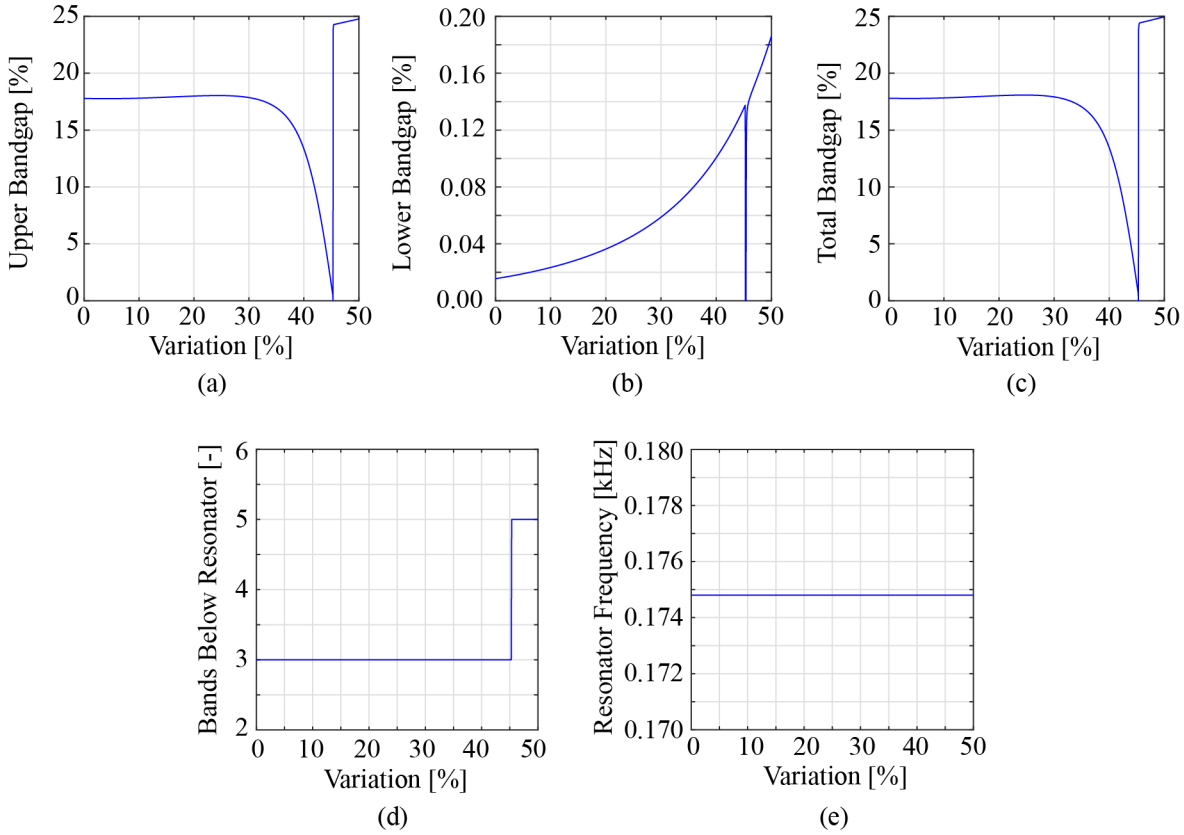

Figure 6.2: **(a)** Upper, **(b)** lower and **(c)** total bandgap for variations between 0% and 50% of the parameters of the matrix beams in the direction in which they increase the lower bandgap. There is a change from 3 to 5 in the **(d)** number of bands below the resonator, and **(e)** the frequency of the resonators is unchanged.

(tables 3.1 and 3.2), and in the other 5 figures the mass density and length of the matrix beams are progressively increased and the Young's modulus of the matrix beams is progressively reduced. All changes are made simultaneously in amounts of 50%, 60%, 70%, 80% and 90% in figures b), c), d), e) and f), respectively. Table 6.1 summarizes the parameters of the 6 configurations used.

From the analysis of the combined effects of the variation of parameters, it can be seen that the case that generates a greater variation in the upper and total bandgap is found in figure 6.1 with a 50% variation of the parameters, while the greater variation of the lower bandgap is shown in figure 6.3 also considering 50% variation. Figure 6.4a shows the dispersion bands of the original configuration used in the parametric analysis, while figures 6.4b and 6.4c show the best case dispersion curves for the upper and lower bandgap, respectively. The results obtained are summarized in table 6.2.

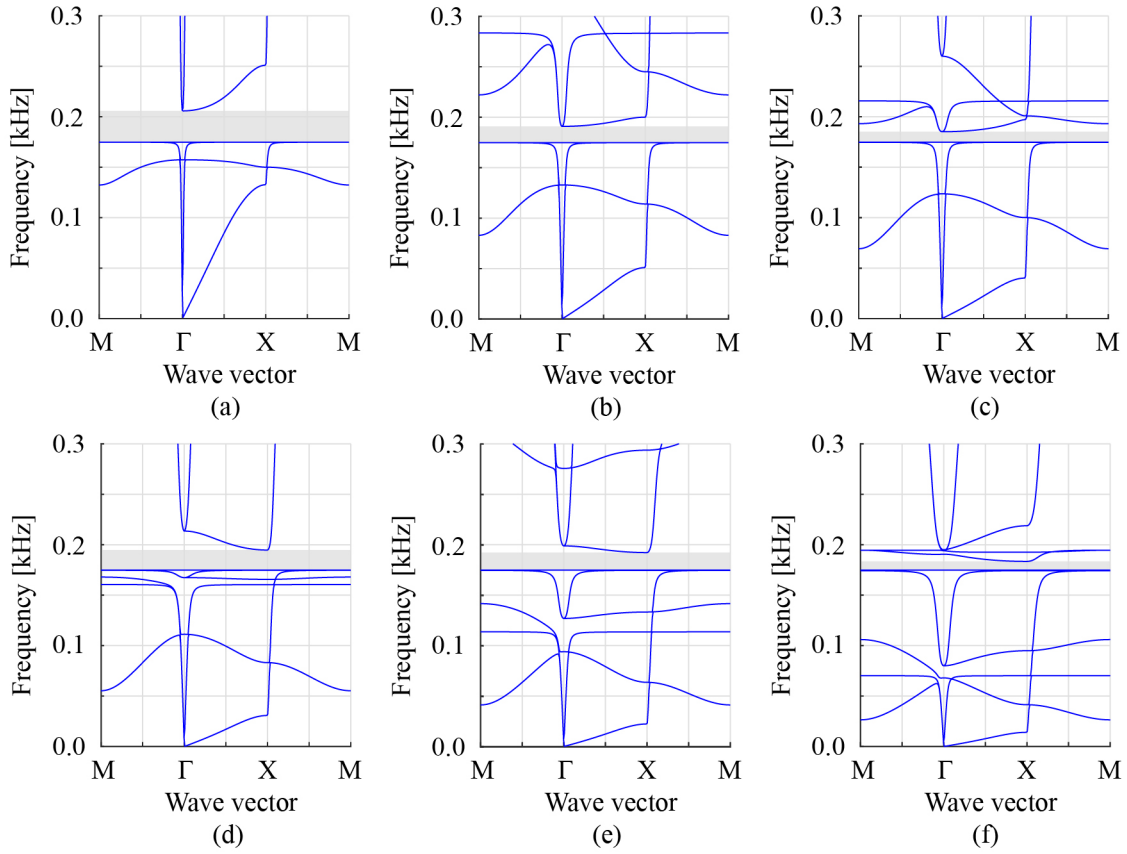

Figure 6.3: Sequence of dispersion diagrams for a type I unit cell exemplifying how certain bands pass below the band associated with resonators. It begins with **(a)** the properties indicated in tables 3.1 and 3.2, and then the mass density and length of the matrix beams are progressively increased and the Young's modulus of the matrix beams is progressively reduced, these changes are made in amounts of **(b)** 50%, **(c)** 60%, **(d)** 70%, **(e)** 80% and **(f)** 90%.

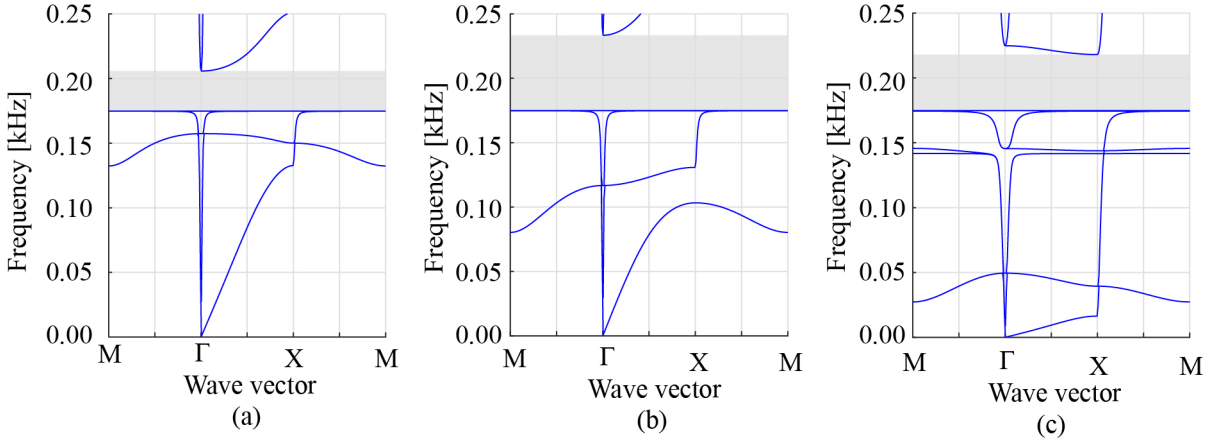

Figure 6.4: Dispersion diagrams for **(a)** the original type I unit cell, the unit cell with the modifications in the matrix beams to enlarge **(b)** the upper bandgap, and **(c)** the lower bandgap.

Table 6.1: Characterization of the bandgaps and the amount of bands below the band of the resonators of the 6 cases presented in the figure 6.3.

Case	Upper bandgap [%]	Lower bandgap [%]	Total bandgap [%]	bands below resonator
a	17.74	0.02	17.76	3
b	9.21	0.05	9.26	3
c	5.96	0.06	6.02	3
d	11.40	0.09	11.49	5
e	9.95	0.14	10.09	5
f	4.97	0.30	5.27	5

Table 6.2: Characterization of the bandgaps and the amount of bands below the band of the resonators of the 3 cases presented in the figure 6.4.

Case	Resonator frequency [Hz]	Upper bandgap [%]	Lower bandgap [%]	Total bandgap [%]	bands below resonator
a	174.80	17.74	0.02	17.76	3
b	174.80	33.50	0.02	33.52	3
c	174.80	24.75	0.19	24.94	5

6.2. Case 2: Optimize bandgap regardless of resonator frequency

To enlarge the upper, lower and total bandgap regardless of the resonator frequency, all parameters must be modified in the direction indicated in section 5.1. Figures 6.1 and 6.2 show the results obtained for the upper and total bandgap optimization, and figures 6.3 and 6.4 shows the results for the lower bandgap.

The case that generates a greater variation in the upper and total bandgap is found in figure 6.5 with a 50% variation of the parameters, while the greater variation of the lower bandgap is shown in figure 6.6 also considering 50% variation. Figure 6.7a shows the dispersion bands of the original configuration used in the parametric analysis, while figures 6.7b and 6.7c show the best case dispersion diagrams for the upper and lower bandgap, respectively. The results obtained are summarized in table 6.3.

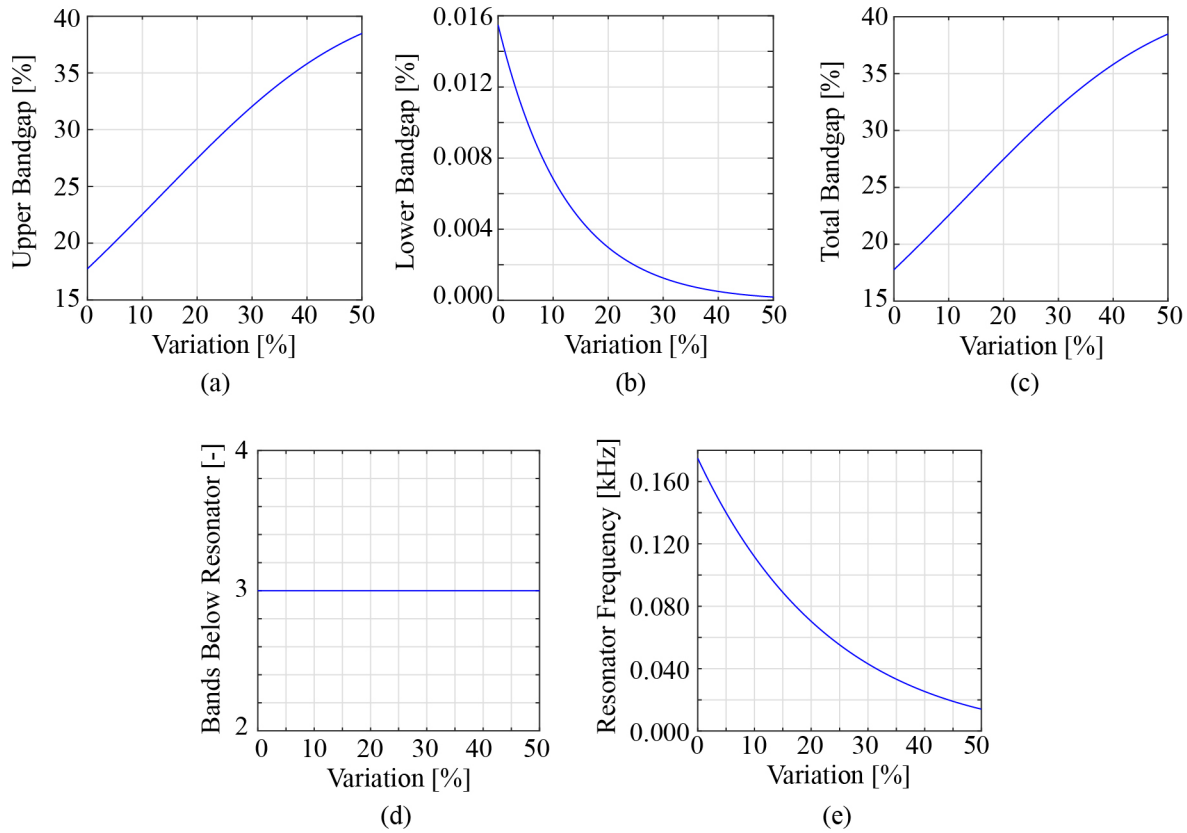

Figure 6.5: **(a)** Upper **(b)**, lower and **(c)** total bandgap for variations between 0% and 50% of all model parameters in the direction in which they increase the upper and total bandgap. The **(d)** number of bands below the resonator remains constant and **(e)** the frequency of the resonators decreases as the variation of the model parameters increases.

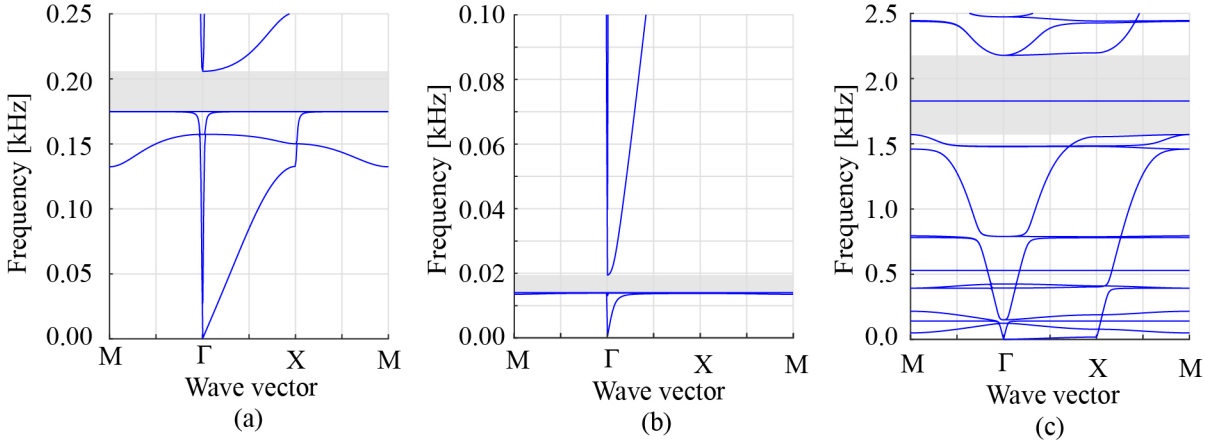

Figure 6.7: Dispersion diagrams for **(a)** the original type I unit cell, the unit cell with the modifications in all the parameters to enlarge **(b)** the upper bandgap, and **(c)** the lower bandgap.

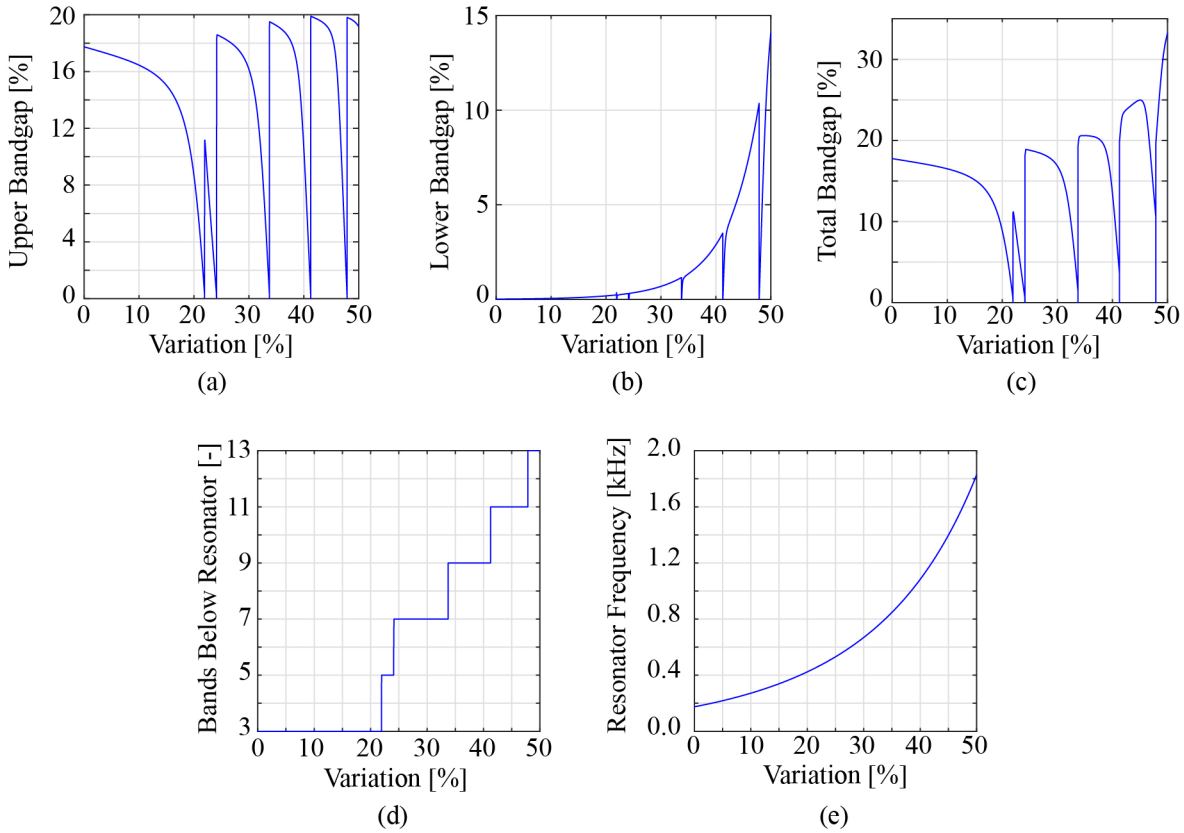

Figure 6.6: **(a)** Upper **(b)**, lower and **(c)** total bandgap for variations between 0% and 50% of all model parameters in the direction in which they increase the lower bandgap. The **(d)** number of bands below the resonator and **(e)** the frequency of the resonators increase as the variation of the model parameters increases.

Table 6.3: Characterization of the bandgaps and the amount of bands below the band of the resonators of the 3 cases presented in the figure 6.3.

Case	Resonator frequency [Hz]	Upper bandgap [%]	Lower bandgap [%]	Total bandgap [%]	bands below resonator
a	174.80	17.74	0.02	17.76	3
b	14.04	38.53	0.00	38.53	3
c	1828.10	19.15	14.08	33.23	13

Chapter 7

FRF for finite panels

In this section, voltage FRFs are simulated for panels panels made up of repetitions of 10x10 unit cells and that are simply supported at their corners. Figure 7.1 shows a scheme of a 10x10 panel obtained from a type I unit cell. Specifically, 3 panels are considered, two of which are formed by type I unit cells (called panel 1 and panel 2), and another formed by type V unit cells (called panel 3). In all cases, coefficients $\gamma_1 = 4.9$ [rad/s] and $\gamma_2 = 1.2 \cdot 10^{-5}$ [s/rad] are considered to add damping to the system.

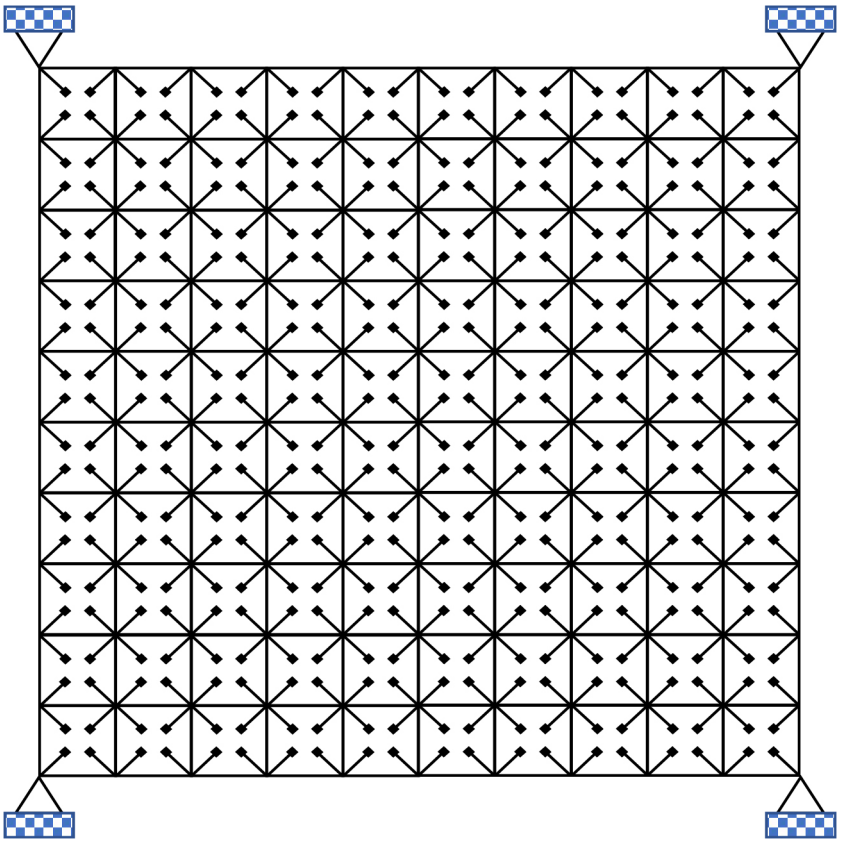

Figure 7.1: Panel of 10x10 repetitions of a type I unit cell with simple support at the corners.

7.1. Case 1: Panels formed by type I unit cells

In this section, 2 panels formed by 10x10 type I cells are analyzed:

- Panel 1: The unit cell used corresponds to the same one used as the starting configuration for the parametric analysis of section 5.1, so the properties of the substructure and PVDF layers are those of tables 3.1 and 3.2, respectively.
- Panel 2: The unit cell used is the one that results from optimizing the bandgap maintaining the frequency of the resonators by modifying the parameters of the matrix, which corresponds to case b of section 6.1 (figure 6.4b).

Figures 7.2a and 7.2b show the voltage FRF and the dispersion diagrams of the type I unit cell associated with panel 1, and figures 7.3a and 7.3b show the results for panel 2. The frequency range covered by the bandgap is indicated by a gray band in both the FRF and the dispersion diagrams. The FRF contains as many curves as there are resonators in the finite panel, since each curve corresponds to the voltage associated with a resonator.

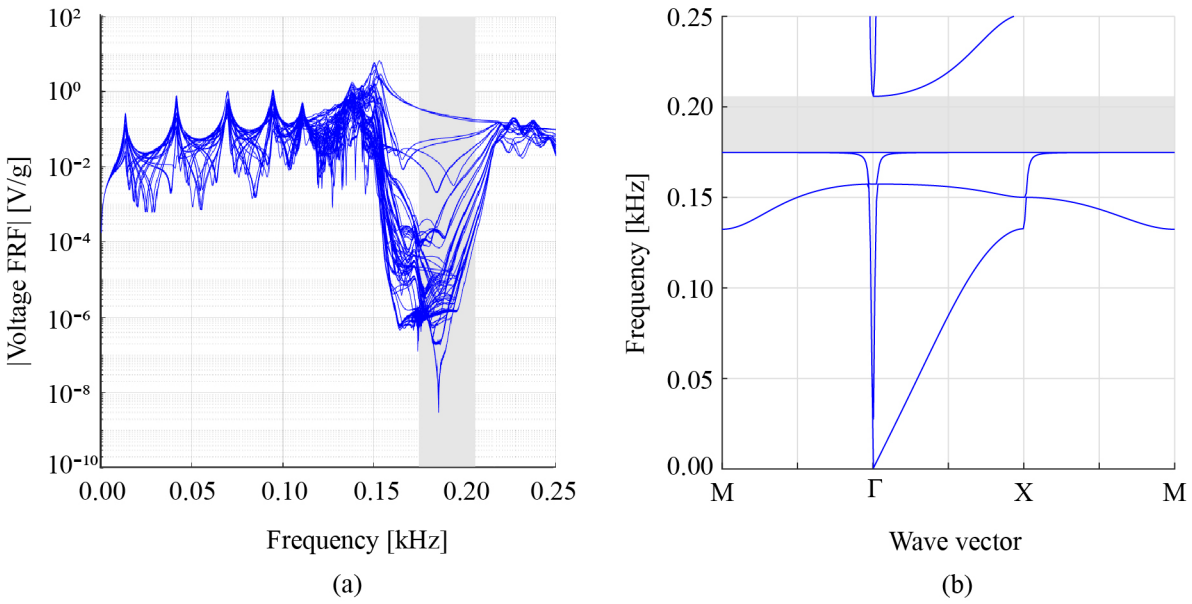

Figure 7.2: **(a)** Voltage FRF for panel 1 and **(b)** dispersion diagram for its type I unit cell.

The results obtained indicate that in the frequency range in which the bandgap occurs, the energy harvesting decreases abruptly, which is consistent with the expected vibration suppression. On the other hand, when modifying the properties of the matrix, the increase in the suppression zone behaves as expected in section 6.1, and is evidenced when comparing figures 7.2a and 7.3a, where the suppression zone is greater in this last.

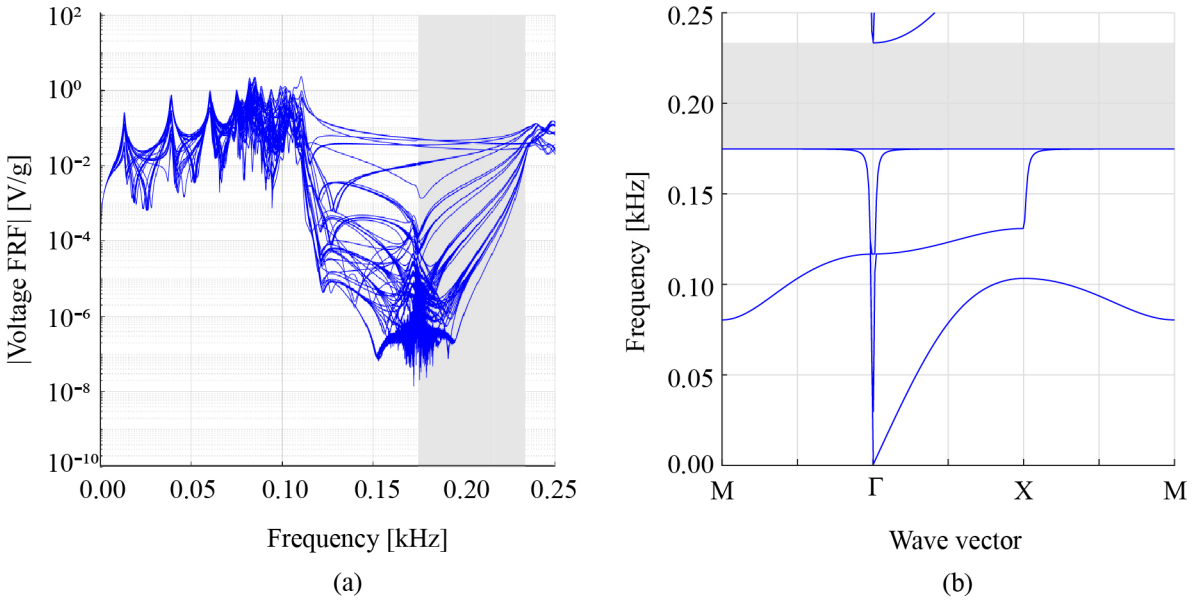

Figure 7.3: **(a)** Voltage FRF for panel 2 and **(b)** dispersion diagram for its type I unit cell.

7.2. Case 2: Panel formed by type V unit cells

An interesting fact occurs when the unit cells present resonators with different natural frequencies, since specific zones of energy harvesting surrounded by zones of vibration suppression can be generated. This means that you can control the areas where energy harvesting and vibration isolation occurs. That is why in this section a 10x10 panel formed from a type V unit cell with two types of resonators is considered. The properties of the matrix beams and one of the resonators of each node are shown in tables 3.1 and 3.2, the other resonator of each node have the same properties but with a tip mass of $0.7M_t$, where M_t is the tip mass of table 3.1.

The results obtained for the panel voltage FRF and the associated unit cell dispersion curves are presented in figures 7.4a and 7.4b, respectively. The results show how there are two bandgaps associated with the resonators, the one with the lower frequency being smaller than the one with the higher frequency, which agrees with the results of section 5.2.

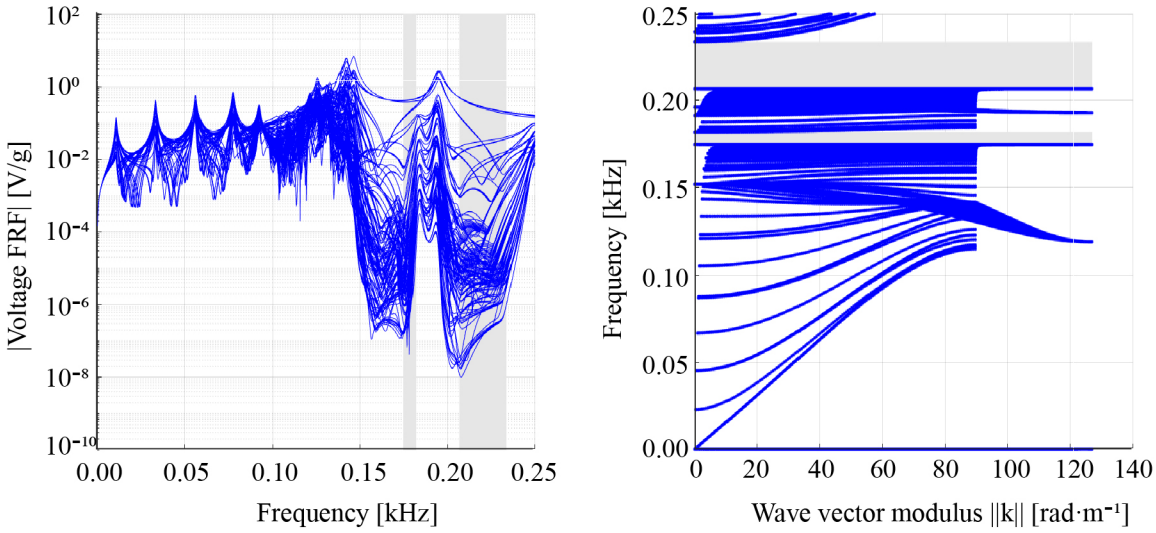

(a) (b)

Figure 7.4: **(a)** Voltage FRF for the 10x10 panel and **(b)** dispersion diagram for its type V unit cell.

Chapter 8

Conclusions

In this study, an electromechanically coupled finite element model is developed using Bernoulli beams applied to periodic structures based on square unit cells with bimorph resonators. Based on this model, multiple simulations are carried out that allow us to conclude on the domain of wave vectors that must be considered to obtain information on the size and position of the bandgap associated with the fundamental frequency of the resonators. With this result, a parametric analysis is performed to see how the model parameters affect the bandgap.

To identify the size and location of the bandgaps associated with local resonances of cantilevers, it is possible to limit the domain of the wave vectors evaluated in the Floquet–Bloch periodic conditions to the vectors N, Y, M, $\bar{X}$ and Γ (see nomenclature in figure 3.5), which can save enormous computational resources if you want to optimize this type of bandgaps. To ensure that the optimization result is adequate, a verification can be carried out by obtaining the dispersion diagram of the optimal configuration using the full BZ.

The bandgaps generated in this work have a large component associated with the upper bandgap and small contributions from the lower bandgaps, this means that obtaining the largest upper bandgap is equivalent to obtaining the largest total bandgap. This phenomenon occurs because the original configuration uses the same materials for the substructure and resonators, and the parameters are varied only within a 50% range around this configuration. To reach larger bandgaps, stiffer resonators and more flexible matrix beams must be considered, which generates an exponential growth of the lower bandgap, and allows its contribution to become greater than that of the upper bandgaps.

The number of bands below the bandgap is not always the same, since it depends on how flexible the matrix beams are with respect to the resonators. Configurations close to the change in the number of bands under the resonator generate abrupt decreases in bandgap. For this reason, if you want to optimize the bandgap, it would be appropriate to perform optimizations leaving the number of bands under the resonator fixed. On the other hand, this can become a relevant issue when materializing a panel, since variations in the nominal properties can lead to abrupt changes in the result, so it is interesting to propagate uncertainties to stay at a point that prevent a large decrease in bandgap.

As future work, a simultaneous optimization of the bandgap and energy harvesting could

be carried out. As a previous step to this optimization, a parametric analysis of the FRF of panels can be done, as was done with the bandgap in this work, to see the way in which the parameters affect the FRF. In general, the results obtained indicate that the electrical parameters do not have a great influence on the bandgap, but they should be much more preponderant in the energy harvesting.

All the analysis was done considering the bandgap associated to the fundamental frequency of the resonators, but bandgaps associated to higher frequencies are also generated, some of which could be interesting to analyze. Furthermore, other extensions of this work could consider parallel connection of piezoelectric layers, use Timoshenko beam-type elements, and/or consider out-of-plane panel motion.

Bibliography

[1] Li, Y., Baker, E., Reissman, T., Sun, C., y Liu, W. K., "Design of mechanical metamaterials for simultaneous vibration isolation and energy harvesting," Smart Materials and Structures, vol. 111, no. 251903, 2017.

[2] Yu, X., Zhou, J., Liang, H., Jiang, Z., y Wu, L., "Mechanical metamaterials associated with stiffness, rigidity and compressibility: A brief review," Progress in Materials Science, vol. 94, pp. 114–173, 2018.

[3] Kochmann, D. M. y Bertoldi, K., "Exploiting microstructural instabilities in solids and structures: from metamaterials to structural transitions," Applied mechanics reviews, vol. 69, no. 5, 2017.

[4] Barchiesi, E., Spagnuolo, M., y Placidi, L., "Mechanical metamaterials associated with stiffness, rigidity and compressibility: A brief review," Mechanics of Solids, vol. 24, no. 1, pp. 212–234, 2019.

[5] Lee, J.-H., Singer, J. P., y Thomas, E. L., "Mechanical metamaterials associated with stiffness, rigidity and compressibility: A brief review," Advanced materials, vol. 24, no. 36, pp. 4782–4810, 2012.

[6] Wang, Q., Jackson, J. A., Ge, Q., Hopkins, J. B., Spadaccini, C. M., y Fang, N. X., "Lightweight mechanical metamaterials with tunable negative thermal expansion," Physical review letters, vol. 117, no. 17, p. 175901, 2016.

[7] Du, Y., Maassen, J., Wu, W., Luo, Z., Xu, X., y Ye, P. D., "Auxetic black phosphorus: a 2d material with negative poisson's ratio," Nano letters, vol. 16, no. 10, pp. 6701–6708, 2016.

[8] Zhao, L., Laredo, E., Ryan, O., Yazdkhasti, A., Kim, H.-T., Ganye, R., Horiuchi, T., y Yu, M., "Ultrasound beam steering with flattened acoustic metamaterial luneburg lens," Applied Physics Letters, vol. 116, no. 7, p. 071902, 2020.

[9] Ma, G. y Sheng, P., "Acoustic metamaterials: From local resonances to broad horizons," Science advances, vol. 2, no. 2, p. e1501595, 2016.

[10] Yang, P., Wu, J., Zhao, R., y Han, J., "Research on local sound field control technology based on acoustic metamaterial triode structure," Crystals, vol. 10, no. 3, p. 204, 2020.

[11] Wang, Y.-F., Wang, T.-T., Liu, J.-P., Wang, Y.-S., y Laude, V., "Guiding and splitting lamb waves in coupled-resonator elastic waveguides," Composite Structures, vol. 206, pp. 588–593, 2018.

[12] Wang, L., Lau, J., Thomas, E. L., y Boyce, M. C., "Co-continuous composite materials for stiffness, strength, and energy dissipation," Advanced Materials, vol. 23, no. 13, pp. 1524–1529, 2011.

[13] Wu, L., Wang, Y., Chuang, K., Wu, F., Wang, Q., Lin, W., y Jiang, H., "A brief review of dynamic mechanical metamaterials for mechanical energy manipulation," Materials Today, 2020.

[14] Fang, X., Wen, J., Bonello, B., Yin, J., y Yu, D., "Ultra-low and ultra-broad-band nonlinear acoustic metamaterials," Nature communications, vol. 8, no. 1, pp. 1–11, 2017.

[15] Cummer, S. A., Christensen, J., y Alú, A., "Controlling sound with acoustic metamaterials," Nature Reviews Materials, vol. 1, no. 3, pp. 1–13, 2016.

[16] Wang, P., Casadei, F., Shan, S., Weaver, J. C., y Bertoldi, K., "Harnessing buckling to design tunable locally resonant acoustic metamaterials," Physical review letters, vol. 113, no. 1, p. 014301, 2014.

[17] Feng, X. y Jing, X., "Human body inspired vibration isolation: beneficial nonlinear stiffness, nonlinear damping nonlinear inertia," Mechanical Systems and Signal Processing, vol. 117, pp. 786–812, 2019.

[18] Li, Y., Baker, E., Reissman, T., Sun, C., y Liu, W. K., "Design of mechanical metamaterials for simultaneous vibration isolation and energy harvesting," Applied Physics Letters, vol. 111, no. 25, p. 251903, 2017.

[19] He, Q. y Jiang, T., "Complementary multi-mode low-frequency vibration energy harvesting with chiral piezoelectric structure," Applied Physics Letters, vol. 110, no. 21, p. 213901, 2017.

[20] Wang, Z., Zhang, Q., Zhang, K., y Hu, G., "Tunable digital metamaterial for broadband vibration isolation at low frequency," Advanced materials, vol. 28, no. 44, pp. 9857–9861, 2016.

[21] Harne, R. L., Song, Y., y Dai, Q., "Trapping and attenuating broadband vibroacoustic energy with hyperdamping metamaterials," Extreme Mechanics Letters, vol. 12, pp. 41–47, 2017.

[22] Manimala, J. M. y Sun, C., "Microstructural design studies for locally dissipative acoustic metamaterials," Journal of Applied Physics, vol. 115, no. 2, p. 023518, 2014.

[23] Hussein, M. I. y Frazier, M. J., "Metadamping: An emergent phenomenon in dissipative metamaterials," Journal of Sound and Vibration, vol. 332, no. 20, pp. 4767–4774, 2013.

[24] Molerón, M., Serra-García, M., y Daraio, C., "Visco-thermal effects in acoustic metamaterials: from total transmission to total reflection and high absorption," New Journal of Physics, vol. 18, no. 3, p. 033003, 2016.

[25] Song, G. Y., Cheng, Q., Huang, B., Dong, H. Y., y Cui, T. J., "Broadband fractal acoustic metamaterials for low-frequency sound attenuation," Applied Physics Letters, vol. 109, no. 13, p. 131901, 2016.

[26] Qi, S., Oudich, M., Li, Y., y Assouar, B., "Acoustic energy harvesting based on a planar acoustic metamaterial," Applied Physics Letters, vol. 108, no. 26, p. 263501, 2016.

[27] Ma, G., Yang, M., Xiao, S., Yang, Z., y Sheng, P., "Acoustic metasurface with hybrid resonances," Nature materials, vol. 13, no. 9, pp. 873–878, 2014.

[28] Madeo, A., Neff, P., Ghiba, I.-D., y Rosi, G., "Reflection and transmission of elastic waves in non-local band-gap metamaterials: a comprehensive study via the relaxed

micromorphic model," Journal of the Mechanics and Physics of Solids, vol. 95, pp. 441–479, 2016.

[29] Ning, S., Yang, F., Luo, C., Liu, Z., y Zhuang, Z., "Low-frequency tunable locally resonant band gaps in acoustic metamaterials through large deformation," Extreme Mechanics Letters, vol. 35, p. 1001623, 2020.

[30] Maugin, G., "On some generalizations of boussinesq and kdv systems," Proc. Estonian Acad. Sci. Phys. Math, vol. 44, no. 1, pp. 40–55, 1995.

[31] Gala, M., Sherbiny, E., y Placidi, L., "Discrete and continuous aspects of some metamaterial elastic structures with band gaps," Archive of Applied Mechanics, vol. 88, no. 10, pp. 1725–1742, 2018.

[32] Boutin, C. y Roussillon, P., "Wave propagation in presence of oscillators on the free surface," International journal of engineering science, vol. 44, no. 3-4, pp. 180–204, 2006.

[33] Miniaci, M., Krushynska, A., Movchan, A. B., Bosia, F., y Pugno, N. M., "Spider web-inspired acoustic metamaterials," Applied Physics Letters, vol. 109, no. 7, p. 071905, 2016.

[34] Li, Z. y Wang, X., "On the dynamic behaviour of a two-dimensional elastic metamaterial system," International Journal of Solids and Structures, vol. 78, pp. 174–181, 2016.

[35] Nouh, M., Aldraihem, O., y Baz, A., "Wave propagation in metamaterial plates with periodic local resonances," Journal of Sound and Vibration, vol. 341, pp. 53–73, 2015.

[36] Bückmann, T., Kadic, M., Schittny, R., y Wegener, M., "Mechanical metamaterials with anisotropic and negative effective mass-density tensor made from one constituent material," physica status solidi (b), vol. 252, no. 7, pp. 1671–1674, 2015.

[37] Hu, J., Yu, T., Yin, S., y Xu, J., "Low-speed impact mitigation of recoverable dna-inspired double helical metamaterials," International Journal of Mechanical Sciences, vol. 161, p. 105050, 2019.

[38] Ba'ba'a, H. A., Attarzadeh, M., y Nouh, M., "Experimental evaluation of structural intensity in two-dimensional plate-type locally resonant elastic metamaterials," Journal of Applied Mechanics, vol. 85, no. 4, p. 041005, 2018.

[39] Thorp, O., Ruzzene, M., y Baz, A., "Attenuation and localization of wave propagation in rods with periodic shunted piezoelectric patches," Smart Materials and Structures, vol. 10, no. 5, p. 979, 2001.

[40] Airoldi, L. y Ruzzene, M., "Wave propagation control in beams through periodic multi-branch shunts," Journal of Intelligent Material Systems and Structures, vol. 22, no. 14, pp. 1567–1579, 2011.

[41] Casadei, F., Delpero, T., Bergamini, A., Ermanni, P., y Ruzzene, M., "Piezoelectric resonator arrays for tunable acoustic waveguides and metamaterials," Journal of Applied Physics, vol. 112, no. 6, p. 064902, 2012.

[42] Bergamini, A., Delpero, T., Simoni, L. D., Lillo, L. D., Ruzzene, M., y Ermanni, P., "Phononic crystal with adaptive connectivity," Advanced Materials, vol. 26, no. 9, pp. 1343–1347, 2014.

[43] Zhou, W., Wu, Y., y Zuo, L., "Vibration and wave propagation attenuation for metama-

terials by periodic piezoelectric arrays with high-order resonant circuit shunts," Smart Materials and Structures, vol. 24, no. 6, p. 065021, 2015.

[44] Hu, G., Tang, L., Banerjee, A., y Das, R., "Metastructure with piezoelectric element for simultaneous vibration suppression and energy harvesting," Journal of Vibration and Acoustics, vol. 139, no. 1, 2017.

[45] Chen, J.-S., Su, W.-J., Cheng, Y., Li, W.-C., y Lin, C.-Y., "A metamaterial structure capable of wave attenuation and concurrent energy harvesting," Journal of Intelligent Material Systems and Structures, vol. 30, no. 20, pp. 2973–2981, 2019.

[46] Ji, J., Luo, Q., y Ye, K., "Vibration control based metamaterials and origami structures: A state-of-the-art review," Mechanical Systems and Signal Processing, vol. 161, p. 107945, 2021.

[47] Shen, L., Wu, J. H., Zhang, S., Liu, Z., y Li, J., "Low-frequency vibration energy harvesting using a locally resonant phononic crystal plate with spiral beams," Modern Physics Letters B, vol. 29, no. 01, p. 1450259, 2015.

[48] Hu, G., Tang, L., y Das, R., "Metamaterial-inspired piezoelectric system with dual functionalities: energy harvesting and vibration suppression," Active and Passive Smart Structures and Integrated Systems 2017, vol. 10164, p. 101641X, 2017.

[49] Hu, G., Tang, L., y Das, R., "Internally coupled metamaterial beam for simultaneous vibration suppression and low frequency energy harvesting," Journal of Applied Physics, vol. 123, no. 5, p. 055107, 2018.

[50] Erturk, A. y Inman, D. J., "A distributed parameter electromechanical model for cantilevered piezoelectric energy harvesters," Journal of Vibration and Acoustics, vol. 130, p. 041002, 2008.

[51] Erturk, A. y Inman, D. J., "An experimentally validated bimorph cantilever model for piezoelectric energy harvesting from base excitations," Smart Materials and Structures, vol. 18, p. 025009, 2009.

[52] De Marqui Junior, C., Erturk, A., y Inman, D. J., "An electromechanical finite element model for piezoelectric energy harvester plates," Journal of Sound and Vibration, vol. 327, pp. 9–25, 2009.

[53] Peralta, P., Ruiz, R. O., y Meruane, V., "Experimental study of the variations in the electromechanical properties of piezoelectric energy harvesters and their impact on the frequency response function," Mechanical Systems and Signal Processing, vol. 115, pp. 469–482, 2019.

[54] Brillouin, L., Wave Propagation in Periodic Structures: Electric Filters and Crystal Lattices. Dover Publications, New York, 2nd ed., 1953.

[55] Maurin, F., Claeys, C., Deckers, E., y Desmet, W., "Probability that a band-gap extremum is located on the irreducible brillouin-zone contour for the 17 different plane crystallographic lattices," International Journal of Solids and Structures, vol. 135, pp. 26–36, 2018.

[56] Hodges, D. H. y Pierce, G. A., Introduction to Structural Dynamics and Aeroelasticity. Cambridge University Press, New York, 2nd ed., 2011.

[57] Lei, X., Wang, Y., Wang, X., Lin, G., y Shi, S., "Revisited on the free vibration of a

cantilever beam with an asymmetrically attached tip mass," Mathematical Problems in Engineering, vol. 2021, 2021.

[58] Ren, B., Cho, H., y Lissenden, C. J., "A guided wave sensor enabling simultaneous wavenumber-frequency analysis for both lamb and shear-horizontal waves," Sensors, vol. 17, no. 488, 2017.